Review

Intrinsic and external active sites of single-atom catalysts

Xue Yao,[1] Ethan Halpren,[1] Ye Zhou Liu,[1] Chung Hsuan Shan,[1] Zhi Wen Chen,[1] Li Xin Chen,[1,*] and Chandra Veer Singh[1,2,*]

SUMMARY

Active components with suitable supports are the common paradigm for industrial catalysis, and the catalytic activity usually increases with minimizing the active component size, generating a new frontier in catalysis, single-atom catalysts (SACs). However, further improvement of SACs activity is limited by the relatively low loading of single atoms (SAs, which are heteroatoms for most SACs, i.e., external active sites) because of the highly favorable aggregation of single heteroatoms during preparation. Research interest should be shifted to investigate SACs with intrinsic SAs, which could circumvent the aggregation of external SAs and consequently increase the SAs loading while maintaining them individual to further improve the activity. In this review, SACs with external or intrinsic SAs are discussed and, at last, the perspectives and challenges for obtaining high-loading SACs with intrinsic SAs are outlined.

INTRODUCTION

Heterogeneous catalysis plays a vital role in energy storage and conversion technologies, such as hydrogen evolution reaction (HER) for hydrogen economy, oxygen reduction reaction (ORR) for metal-air batteries, and nitrogen reduction reaction (NRR) for green NH_3 synthesis, holding great promise to accelerate a sustainable future.[1–5] Developing high-performance catalysts is the prerequisite for industrializing a specific catalytic process, and currently many industrial catalysts are metal particles supported on solid surfaces.[6–8] The catalytic efficiency of heterogeneous catalysts is highly related to the surface/volume ratio of active components, and the specific activity per atom usually increases with decreasing the particle size. Much effort has been devoted to downsizing metal particles to achieve better catalytic performance.[9–13] The ultimate limit for downsizing metal particles is single-atom catalysts (SACs), where highly dispersed metal single atoms (SAs) are anchored on the surface of solid supports (Figure 1A). The first practical SAC with Pt SAs supported on iron oxide (Pt_1/FeO_x) was reported in 2011,[14] and it shows higher activity toward CO oxidation than the cluster/particle counterpart. Another advantage of SACs is the precisely identified and uniform active sites, which is conducive to revealing the catalytic mechanism. Such an advantage used to be only owned by homogeneous catalysts, of which the application is limited by the poor stability and recyclability. SACs bridge the gap between homogeneous and heterogeneous catalysis. Since then, SACs have attracted extensive research attention because of the excellent catalytic performances.[15–39]

Over the last decade, large amounts of SACs have been synthesized and utilized toward catalytic reactions including HER, ORR, and NRR, and many good reviews have summarized the design concept, synthesis, and application of SACs from both the experimental and theoretical sides.[12,40–48] For example, Zhuo et al. focused on the stability of metal SAs anchored on different sites of graphene support and the intrinsic connection between theoretical understanding on electronic structures and catalytic properties[40]; Wang et al. summarized the concept of SACs with two-dimensional (2D) supports for catalysis and pointed out the interplay between the unique geometric and electronic structures of 2D supports and the catalytic performance of confined single active sites[42]; Li et al. discussed the computational simulations on a couple of important applications of SACs and provided good perspectives on future computational simulations for SACs.[43] Increasing the SAs loading while maintaining SAs as individual sites is the grail to achieve better catalytic performances (Figure 1A). However, SAs are heteroatoms for most SACs,[15–32] even for most metal-organic frameworks (MOFs)-derived carbon-based SACs,[34–38] where vacancies are first created on support surface and then used to capture single heteroatoms (Figure 1B). In this case, SAs are regarded as external active sites herein. Owing to the high surface energy of single heteroatoms compared to
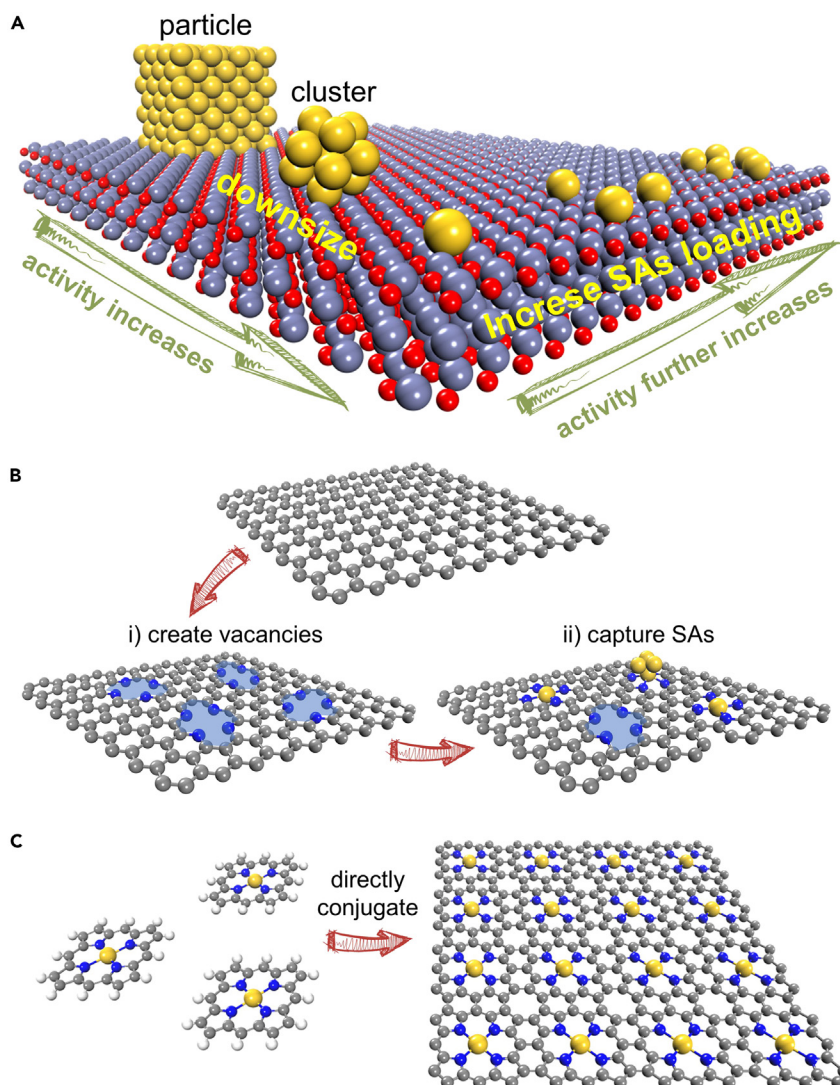
Figure 1. External and intrinsic SAs in carbon-based SACs

(A–C) Schematic illustrations of the increase in catalytic activity by downsizing the active component and the further increase by increasing the SAs loading (A), the common approach to synthesize carbon-based SACs with the active center of M_1N_4: (i) create vacancies and (ii) capture single heteroatoms (i.e., external SAs) (B), and the conjugation of MTP molecules having natural M_1N_4 centers to SACs with high-loading intrinsic SAs (C).

cluster/particle counterparts, the self-nucleation process of external SAs occurs very easily during preparation. Aiming at circumventing the self-nucleation of external SAs, the precursors of SAs should be controlled at a low concentration, resulting in the relatively low loading of external SAs (typically <2 wt % on non-carbon supports).[14,16,49–51] Hence, it is worthy to shift research interest to SACs with intrinsic SAs. Figure 1C gives an example of intrinsic SAs with the same active centers in Figure 1B (M_1N_4, M: transition metal) to illustrate the difference between external and intrinsic SAs. Metalloporphyrin (MTP) molecules have natural M_1N_4 centers (Figure 1C, left), rather than capture single heteroatoms to construct M_1N_4 centers. After the direct conjugation of MTP molecules to 2D sheets (Figure 1C, right), SACs with high-loading intrinsic SAs can be synthesized.

In this contribution, we discuss the recent advances in SACs with external and intrinsic SAs. First, SACs with external SAs, including noble and non-noble metals as well as non-metal atoms, are summarized, and the corresponding loading/density of external active sites is discussed. Then, we discuss some studies on SACs with intrinsic SAs, which is a promising field because of the great advantages in achieving high-loading SAs

and high catalytic performance but rarely summarized. In the discussion sections, the applications of SACs in thermocatalysis, electrocatalysis, and photocatalysis are involved. Finally, the perspectives and challenges on SACs with high-loading intrinsic SAs are outlined.

SACs WITH EXTERNAL SAs

Catalytic performances of SACs are determined by both SAs and supports. The interactions between SAs and supports have great impact on the electronic structure of SAs, and consequently regulating the coordination environment of SAs is highly efficient in tailoring the activity and selectivity. By sufficient and fine regulations, SAs could be totally different from the elemental bulk counterpart, showing excellent activity/selectivity. The application of SACs determines what kind of supports should be utilized. In detail, high-conductivity supports, such as carbon-based materials, are desirable for electrocatalysis, whereas high stability and suitable bandgap are required for thermocatalysis and photocatalysis, respectively.

NOBLE METAL SAs

State-of-the-art catalysts for HER, oxygen evolution reaction (OER), etc., mainly rely on noble metals, such as Pt, Pd, Ru, Ir.[52–55] Since noble metals are scarce and expensive, making the best of the noble resources is a big but challenging task for industrial catalysis. Increasing the efficiency of Pt is a significant innovation for the first practical SACs, Pt_1/FeO_x.[14] Using the co-precipitation method, a catalyst with Pt SAs anchored onto the defects of FeO_x surfaces (sample A, the Pt loading of 0.17 wt %), as well as a similar catalyst with the Pt loading of 2.5 wt % (sample B), was synthesized. The aberration-corrected high-angle annular dark-field scanning transmission electron microscopy (HADDF-STEM) images (Figures 2A and 2B) suggested that only Pt SAs can be seen in sample A, whereas Pt SAs, 2D Pt rafts, and three-dimensional Pt clusters coexist in sample B. In the extended X-ray absorption fine structure (EXAFS) spectra (Figure 2C), sample A has a strong peak at ∼ 1.7 Å from the Pt-O contribution and a weak peak at ∼ 2.5 Å from the Pt-Pt or Pt-Fe contribution, further suggesting that sample A contains only Pt SAs. Moreover, Pt SAs in sample A carry positive charges, whereas Pt^0 clusters are dominant in sample B according to the normalized X-ray absorption near-edge structure (XANES) spectra (Figure 2D). *In situ* Fourier-transform infrared (FTIR) spectroscopy was used to explore the dispersion and oxidation state of Pt. The band related to CO adsorbed on $Pt^{\delta+}$ (2080 cm^{-1}, Figure 2E) indicated the isolation of Pt SAs in sample A, whereas the bands for linearly bonded CO on Pt^0 sites (1860, 1950, and 2030 cm^{-1}, Figure 2F) verified the existence of Pt dimers or clusters in sample B. Owing to the highly dispersed Pt SAs, sample A exhibited higher catalytic performances toward CO oxidation and preferential oxidation than sample B and the standard Au/Fe_2O_3 catalyst. The same group also synthesized a series of catalysts with different Ir loadings (0.01, 0.22, 0.32, and 2.40 wt %) on FeO_x supports.[56] Similar to Pt_1/FeO_x, Ir clusters and particles were formed with increasing Ir loading (Figure 3A). The as-prepared Ir_1/FeO_x SAC with the Ir loading of 0.01 wt % exhibited high activity for water gas shift reaction (CO + H_2O → CO_2 + H_2), and the theoretical contribution from Ir SAs to the total CO conversion was claimed to be around 70% based on the weight percentage of Ir SAs (Figure 3B). These two pioneering works demonstrate the successful synthesis of promising catalysts with minor usage of noble metals and the importance of SAs compared with the cluster and nanoparticle counterparts. Later, Pd_1/FeO_x,[57,58] Rh_1/FeO_x,[57] Au_1/FeO_x,[57,59] and Ru_1/FeO_x[60] were synthesized as well; Pt_1/FeO_x and Ir_1/FeO_x were also used in NO reduction,[61] nitroarenes hydronation,[62] oxygen activation,[63] etc.

Inspired by the high performances of Pt_1/FeO_x and Ir_1/FeO_x,[14,56] SACs with atomically dispersed earth-scarce noble metals have attracted increasing research attention to create more cost-effective catalysts.[64–68] These SACs indeed exhibited high catalytic performances, but the loading of SAs is relatively low, e.g., 0.17 and 0.01 wt % for Pt_1/FeO_x and Ir_1/FeO_x,[14,56] respectively. To increase the loading of noble metal SAs, Liu et al. reported a room-temperature photochemical strategy to fabricate atomically dispersed Pd catalyst on TiO_2 nanosheets (Pd_1/TiO_2) with the Pd loading up to 1.5 wt %.[69] They first synthesized two-atom–thick TiO_2 nanosheets stabilized by ethylene glycolate (EG) and then dispersed them into water with H_2PdCl_4 solution under ultraviolet (UV) treatment. The TEM and HAADF-STEM images and the results of energy-dispersive X-ray spectroscopy (EDS) mapping, XANES and EXAFS spectrometry, FTIR spectra of CO adsorption suggested that Pd SAs are highly dispersed in the as-prepared Pd_1/TiO_2 catalyst even when the Pd loading increases to 1.5 wt %. The Pd_1/TiO_2 catalyst exhibited extremely high catalytic activity and stability toward styrene hydrogenation compared with the commercial Pd/C catalyst and the unsupported homogeneous H_2PdCl_4 catalyst (Figures 3C and 3D). During preparation, the UV-induced formation of EG radicals on TiO_2 promoted the Cl^- removal (Figure 3E), which is beneficial to the high performance of Pd_1/TiO_2. The $PdCl_2/TiO_2$ catalyst synthesized by the same method as for Pd_1/TiO_2
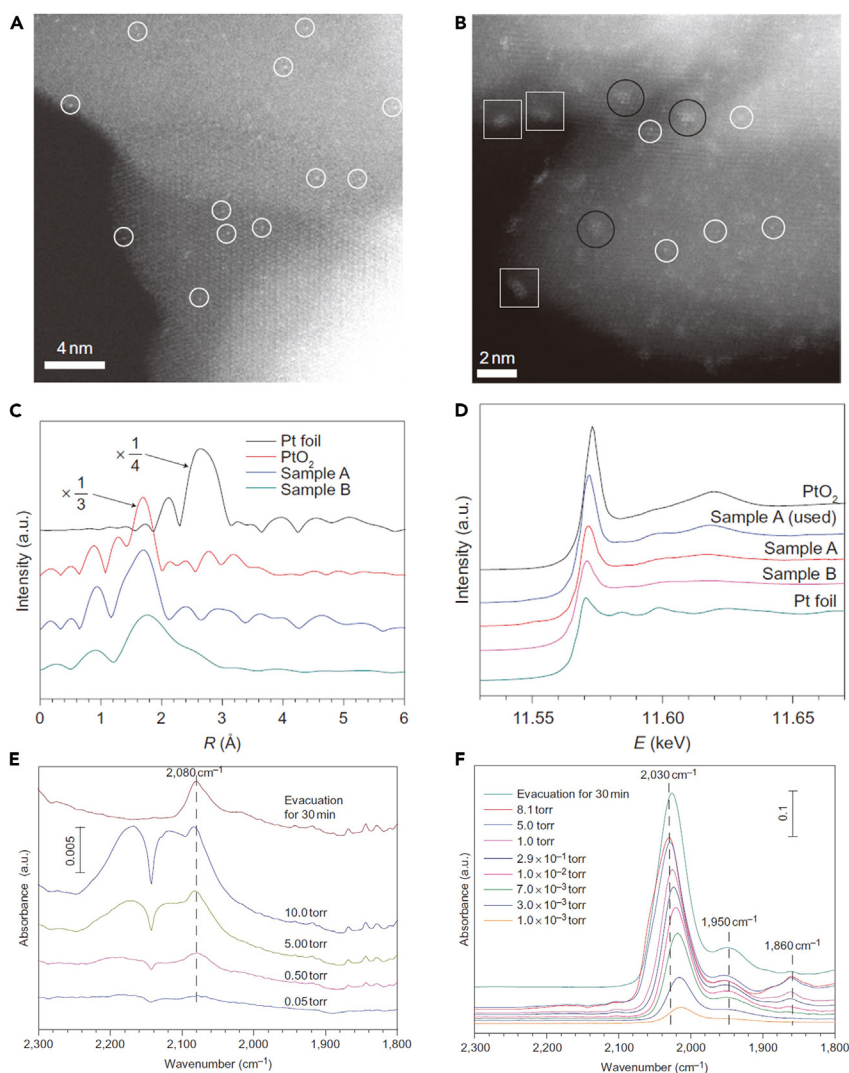
Figure 2. Characterizations of the first practical SAC
(A and B) HAADF-STEM images of sample A (A) and sample B (B).
(C–D) The Fourier transform spectra from EXAFS (C) and the normalized XANES spectra (D) of sample A, sample B, PtO_2, and Pt foil.
(E–F) *In situ* FTIR spectra of CO adsorption for sample A (E) and sample B (F).
(A–F) Reproduced with permission.[14] Copyright 2011, Nature Publishing Group.

but without the UV treatment showed poorer catalytic performance than Pd_1/TiO_2. Han et al. modified such a photochemical method and synthesized a Pt_1/TiO_2 catalyst with the Pt loading of 1 wt %.[70] Using *in situ* diffuse reflection infrared Fourier transform spectroscopy (DRIFTs) and *in situ* XANES spectroscopy, they found that the strong metal-support interaction (SMSI) can also occur between Pt SAs and TiO_2 at the reduction temperature of 600°C, whereas the SMSI between Pt nanoparticles and TiO_2 occurred at 250°C (Figures 3F and 3G). Moreover, Pt SAs were confirmed to be the true active sites toward the hydrogenation of 3-nitrostyrene. SACs with increasing SAs loading are promising catalysts, which have not only high activity but also high catalytic capability that conventional catalysts do not possess. With TiO_2 as the support, Guo et al. used the ball milling method to synthesize the Pd_1/TiO_2 catalyst and utilized it to catalyze the photo-thermo semi-hydrogenation of acetylene, where the photo-induced electrons transferred from TiO_2 support to the adjacent Pd SAs facilitated the activation of acetylene[71]; Tang et al. synthesized a Rh_1/TiO_2 catalyst and demonstrated that Rh SAs can change their structures and adapt their catalytic sites under reaction conditions[72]; Thang et al. explained that the high thermal stability of the Pt_1/TiO_2 catalyst
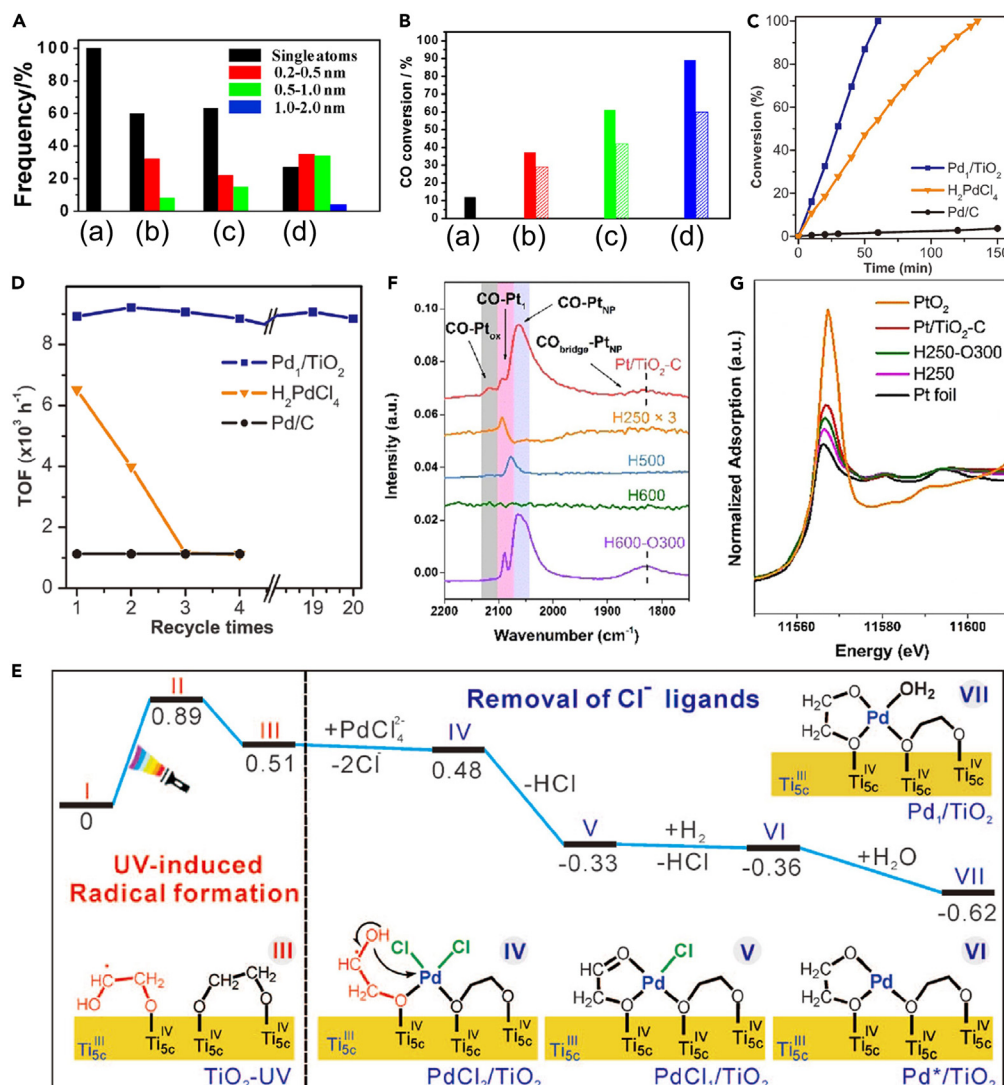
Figure 3. Noble metal SACs with external Ir, Pd, and Pt SAs

(A and B) The frequencies of the observed size scope (A) and the differences between the experimental CO conversions at the steady state (solid) and the estimated ones based on the contributions from Ir SAs (stripe) (B) of Ir/FeO$_x$ catalysts with the Ir loadings of 0.01 (a), 0.22 (b), 0.32 (c), and 2.40 wt % (d). (A and B) Reproduced with permission.[56] Copyright 2013, American Chemical Society.

(C and D) Catalytic performances for the first run (C) and turnover frequency (TOF) (D) of several recycles for Pd$_1$/TiO$_2$, H$_2$PdCl$_4$, and commercial Pd/C.

(E) Energies and models of intermediates and transition states in the stepwise preparation mechanism of Pd$_1$/TiO$_2$.

(C–E) Reproduced with permission.[69] Copyright 2016, American Association for the Advancement of Science.

(F and G) *In situ* DRIFT (F) and XANES spectra (G) of different Pt/TiO$_2$ samples.

(F–G) Reproduced with permission.[70] Copyright 2020, Wiley-VCH Verlag GmbH & Co. KGaA, Weinheim.

through oxidative and reductive treatments is because every Pt SA binds to two excess O atoms, forming PtO$_2$ on surface.[73]

NON-NOBLE METAL SAs

Although noble metals usually act well in catalyzing a specific reaction, non-noble metals also play a vital role in catalysis, such as Fe-based catalysts for the Haber-Bosch process, a method for industrial NH$_3$ synthesis.[74–77] For metal SAs, their properties change significantly and are even no longer similar to the elementary bulk counterparts, further indicating the great potential of SACs with non-noble metal SAs.
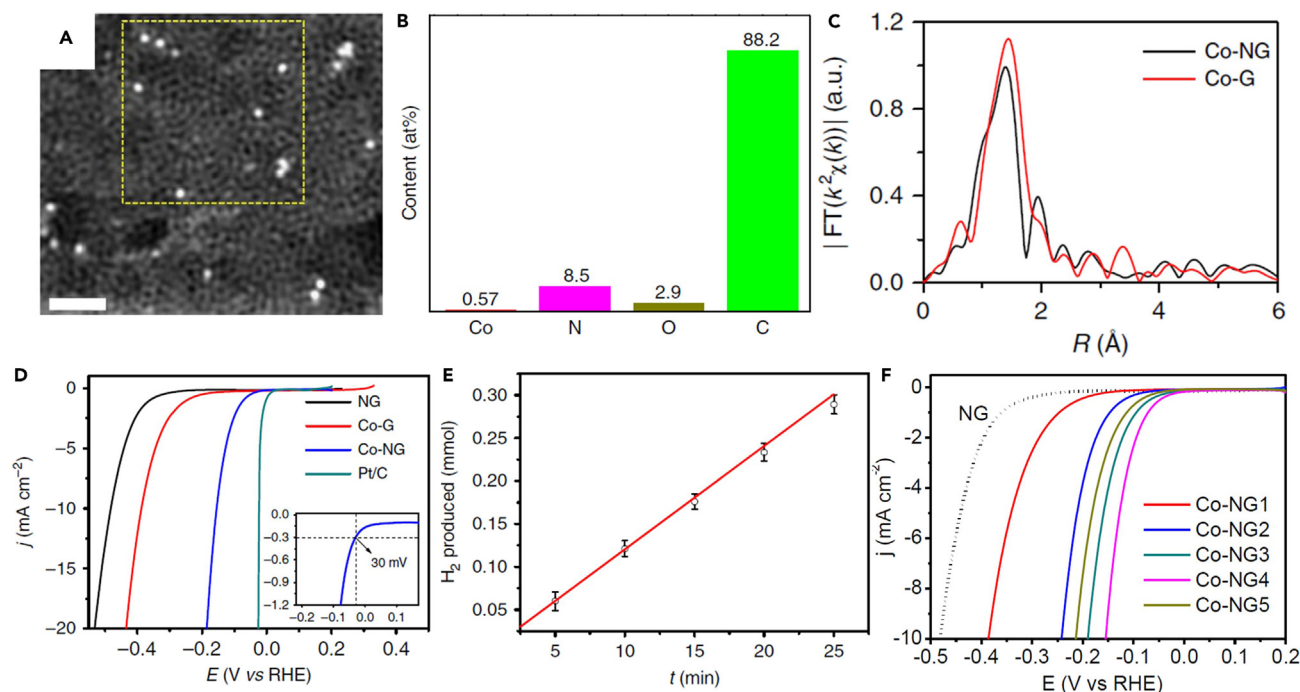
Figure 4. Non-noble metal SACs with external Co SAs

(A) HAADF-STEM image of the Co-NG catalyst with the scale bar of 1 nm.

(B) Percentages of Co, N, O, and C in the Co-NG catalyst measured by XPS and ICP-OES.

(C) The k^2-weighted EXAFS in k-space for Co-NG and Co-G.

(D) LSVs of NG, Co-G, Co-NG, and Pt/C in 0.5 M H_2SO_4 at the scan rate of 2 mV s^{-1}.

(E) The molar number of produced H_2 as a function of time, where the red line denotes the theoretically calculated amounts of H_2 with 100% Faradaic efficiency.

(F) LSV polarization curves for catalysts with the Co loading of 0.03 (Co-NG1), 0.09 (Co-NG2), 0.29 (Co-NG3), 0.57 (Co-NG4), and 1.23 (Co-NG5).

(A–F) Reproduced with permission.[81] Copyright 2015, Nature Publishing Group.

Using the machine learning (ML) techniques, Wu et al. predicted the catalytic performances of carbon-based SACs toward OER and ORR and found that SACs with non-noble metal SAs were superior,[78,79] which also occurs for double-atom catalysts (DACs).[80] To circumvent the limitation of high cost of Pt catalysts toward HER, Fei et al. synthesized a Co SAC (Co-NG) with Co SAs on N-doped graphene oxide (GO), which exhibited extraordinarily high catalytic performance toward HER in both acidic and basic media.[81] GO and cobalt salts were sonicated with the weight ratio of GO:Co = 135:1, and then the well-mixed precursor solution was freeze-dried and heated, which indicates an inexpensive, concise, and scalable method to synthesize non-noble metal SACs. The HAADF-STEM image (Figure 4A) clearly showed Co SAs in the carbon matrix, and the contents of Co, N, O, and C in Co-NG were determined to be 0.57, 8.5, 2.9, and 88.2 at%, respectively, by the inductively coupled plasma optical emission spectrometry (ICP-OES, Figure 4B). The EXAFS analysis was performed at the Co K-edge using the Fourier transform (FT) (Figure 4C) to further confirm the individual Co SAs in Co-NG. The linear sweep voltammograms (LSVs) results in acidic 0.5 M H_2SO_4 media (Figure 4D) suggested that Co-NG is superior HER catalyst though slightly poor as compared to the commercial Pt/C catalyst, and the Faradaic efficiency of the Co-NG catalyst was determined to be ~100% (Figure 4E). The Co-NG catalyst also exhibited high HER activity when tested in alkaline 1 M NaOH media. Moreover, Co-NG catalysts with different Co loadings (from 0.03 to 1.23 at%) were synthesized, and the HER activity did not always increase with the increasing Co loading (Figure 4F). This can be ascribed to that not all Co atoms can be incorporated into the N-doped graphene matrix and consequently Co-containing clusters or particles occur. This Co-NG catalyst is the first inorganic solid-state SAC exhibiting excellent catalytic performance toward HER, proving that non-noble metal SACs hold great promise to replace noble metal-based catalysts.

MOFs are a class of porous crystalline materials consisting of metal-containing nodes and organic linkers. Owing to the natural single-atom metal sites separated by linkers, MOFs have been widely studied as
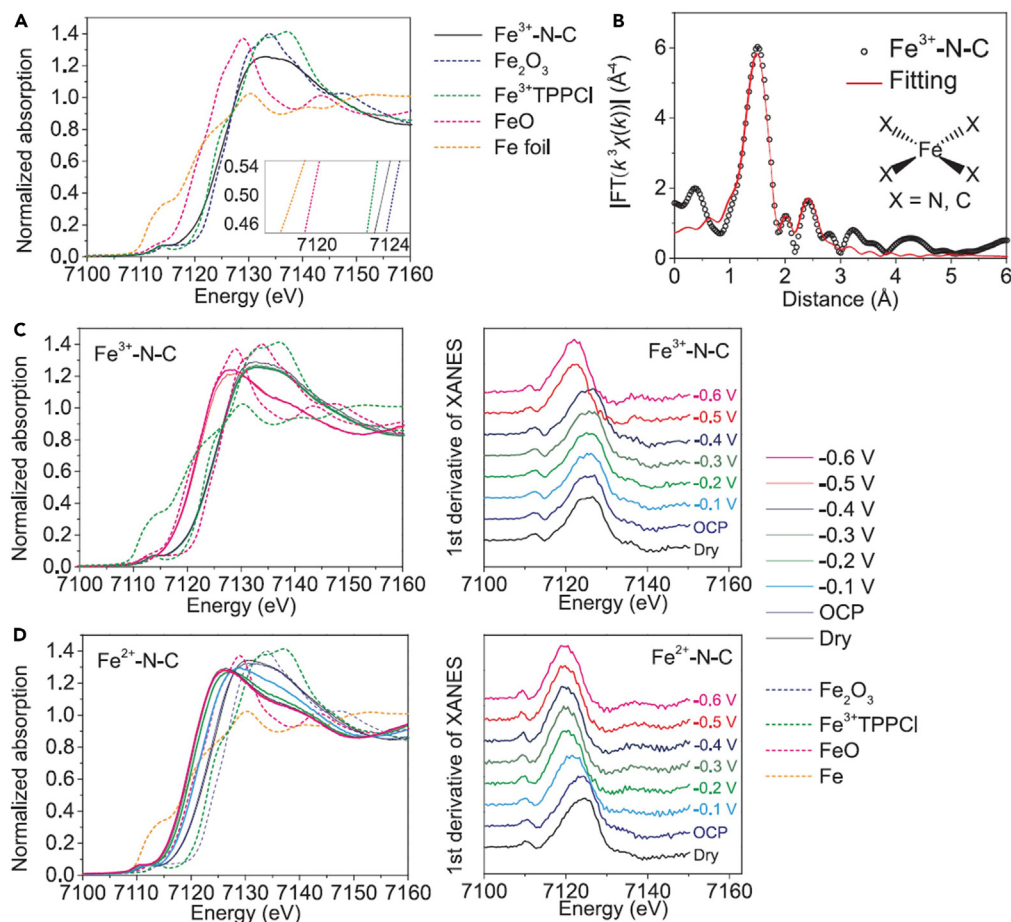
Figure 5. MOF-derived SACs with external Fe SAs

(A) Fe K-edge XANES spectra of Fe^{3+}-N-C, Fe_2O_3, Fe^{3+}TPPCl, FeO, and Fe foil.

(B) R-space Fe K-edge EXAFS spectra.

(C and D) Fe K-edge XANES spectra (left) and the first derivative of the spectra (right) of Fe^{3+}-N-C (C) and Fe^{2+}-N-C (D) as dry powder (black) and loaded on glassy carbon electrodes at open circuit potential (OCP) (blue), −0.1 to −0.6 V versus RHE, with the spectra of Fe_2O_3, Fe^{3+}TPPCl, FeO, and Fe foil as references.

(A–D) Reproduced with permission.[38] Copyright 2019, American Association for the Advancement of Science.

templates/precursors for noble metal and non-noble metal SACs.[33–38] In MOFs and derivates, SAs can be introduced into the metal nodes, organic linkers, or pores, and SACs (mainly M_1N_x-C catalysts) can be synthesized after the high-temperature pyrolysis. However, for most MOFs and derivates with SAs stabilized by linkers or pores, vacancies in (N-doped) carbon matrix generated by the evaporation of low-boiling point metal sites are still required to capture SAs. In this case, SAs are still external. Hence, only SAs introduced into the metal nodes of MOFs and derivates, i.e., mixed metal nodes, can be regarded as intrinsic, of which the coordination environment (at least the first-shell coordination) is unchanged before and after pyrolysis. Gu et al. synthesized Fe^{3+}-N-C catalyst with the Fe loading of 2.8 wt % by the pyrolysis of Fe-doped ZIF-8, where SAs were stabilized in pores, and investigated its properties and performance by operando techniques.[38] The Fe K-edge XANES spectrum (Figure 5A) suggested that Fe ions in the as-prepared Fe^{3+}-N-C catalyst are in the +3 oxidation state, and the Fe K-edge EXAFS spectrum (Figure 5B) indicated that Fe^{3+} sites adopt a Fe_1X_4 (X = N or C) structure. The operando X-ray absorption spectroscopy measurements were performed to explore the change of the Fe^{3+}-N-C catalyst during the CO_2 reduction reaction (CO_2RR). The Fe^{3+} sites were reduced to Fe^{2+} sites with the decreasing applied potential (Figure 5C), along with the first-shell coordination number of Fe ions decreased from 4 to 3. The Fe^{2+}-N-C catalyst was also prepared, where Fe^{2+} sites coordinated with four pyridinic N atoms (pyrrolic N atoms for Fe^{3+} sites in Fe^{3+}-N-C), and there also existed important number of Fe^{3+} sites in Fe^{2+}-N-C. The in situ XANES analysis suggested that Fe^{3+} sites in the Fe^{2+}-N-C catalyst are reduced to Fe^{2+} at −0.1 to −0.2 V versus RHE (Figure 5D).
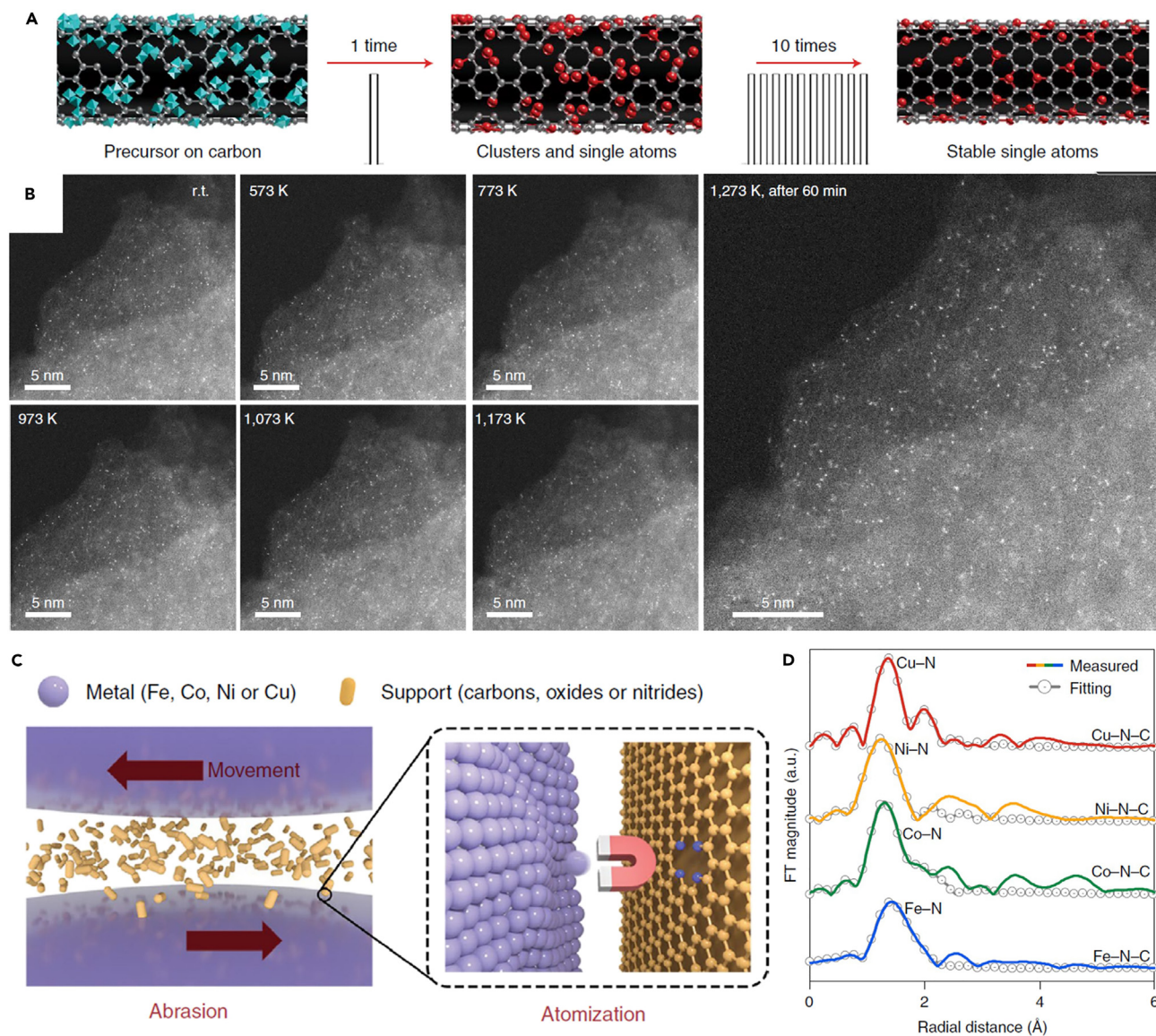
Figure 6. Strategies to synthesize SACs with external metal SAs

(A) Schematic diagram of the synthesis and dispersion process of SACs by the high-temperature shockwave.

(B) *In situ* STEM images of the representative Pt SACs from room temperature up to 1273 K.

(A and B) Reproduced with permission.[32] Copyright 2019, Nature Publishing Group.

(C) Schematic diagram of SACs formation by the mechanochemical abrasion.

(D) The radial distribution functions of the as-prepared Fe-N-C, Co-N-C, Ni-N-C, and Cu-N-C catalysts.

(C and D) Reproduced with permission.[16] Copyright 2022, Nature Publishing Group.

The activity and stability of Fe^{2+}-N-C catalyst were both poorer than the Fe^{3+}-N-C catalyst. This work proves the significant impact of the coordination environment of SAs in catalytic performances.

Co and other non-noble metal (Fe, Ni, Cu) SACs can be also synthesized by the high-temperature shockwave method and the mechanochemical abrasion method.[16,32] In the high-temperature shockwave method, defects in supports can capture SAs generated by the on-state shockwave heating, and the off-state ensures the stability of whole system (Figure 6A). *In situ* STEM images (Figure 6B) confirmed that SAs have a superior structural stability and remain single from room temperature up to 1273 K. Using this method, noble metal SACs, e.g., Pt SACs with the Pt loading of ~0.24 wt %, can be synthesized as well, and the support can be carbon materials and TiO_2. As regards the mechanochemical abrasion

method, SAs abraded from the corresponding elementary bulk metals were also stabilized by defects in supports (Figure 6C). Taking the as-prepared carbon-based SACs as the example, the EXAFS results suggested that Cu, Co, Ni, and Fe exist in the single-atom state (Figure 6D). The Fe loading in the Fe-N-C SAC reached ∼1.10 ± 0.3 wt %, and the SAs loading can be tuned by changing the abrasion rate. Similar to the universality of the high-temperature shockwave method, this method was also useful to synthesize SACs with the support of C_3N_4, MgO, SiO_2, CeO_2, etc. These newly developed SACs preparation methods suggest the important role of support defects in capturing single heteroatoms.

NON-METAL SAs

Industrial catalysis heavily relies on metal-based catalysts, such as Fe-based catalysts for industrial NH_3 synthesis.[74–77] Moreover, natural N_2 fixation is achieved by nitrogenases, where the active sites are also transition metals, mainly Mo and V.[82–84] Compared to metal compounds, metal-free materials are recently emerging as highly promising catalytic candidates because of their abundant natural resources, stability in acidic and/or alkaline environment, and environmental friendliness.[85–90] Taking N_2 fixation as the example, the underlying reason why metal compounds are efficient in binding and activating N_2 molecule is the advantageous combination of unoccupied and occupied d orbitals, which can synergically accept electrons from and back-donate to N_2 molecules, i.e., the "accept and back-donate" mechanism (Figure 7A). Recently, Légaré et al. found that some boron-contained compounds are also active for N_2 fixation, where boron sites can be active centers because of the combination of filled and empty p orbitals (Figure 7A).[91] Yu et al. extended this concept to heterogeneous catalysis and synthesized boron-doped graphene (BG) with boron SAs on graphene (G) by the thermal reduction of H_3BO_3 with GO in a mixed H_2/Ar gas.[92] The highest occupied molecular orbital (HOMO) and the unoccupied molecular orbital (LUMO) of G were non-localized and symmetric, but both HOMO and LUMO of BG were redistributed (Figure 7B). The redistribution of electron densities resulted in positively charged boron SAs in BG samples, which is in favor of N_2 adsorption. There were four structures of boron SAs, including BC_4, BC_3, BC_2O, and BCO_2 (Figure 7C), and their proportions were different in BG samples (Figure 7D). Only physical N_2 adsorption was observed for G, and chemical N_2 adsorption was present for BG samples (Figure 7E). Moreover, the chemical N_2 adsorption on BG samples increased as the boron loading increases, suggesting that chemical N_2 adsorption sites are boron SAs. The BG-1 sample with the highest boron loading of 6.2 at% exhibited higher performance toward NRR than other BG samples and other reported NRR catalysts in aqueous solutions at ambient conditions.[93–97] This work provides strong evidence of the broad applications of SACs with the active sites of non-metal SAs.

Inspired by the high performance toward NRR of the experimentally synthesized boron SACs,[92] the theoretical design of boron SACs toward NRR became active. The boron sites in homogeneous catalysts with sp^2 hybridization have been proved to be efficient in N_2 fixation (Figure 7A).[91] Ling et al. analyzed that boron sites with sp^3 hybridization could also act as active centers for N_2 fixation because of the concurrence of occupied and empty p orbitals and N_2 molecules could be adsorbed with the side-on configuration on boron sites.[98] They designed a metal-free SAC, boron-doped graphitic-carbon nitride (B/g-C_3N_4), toward photocatalytic NRR, where g-C_3N_4 was chosen because of its broad applications in photocatalysis with the suitable bandgap.[99–101] The as-designed B/g-C_3N_4 catalyst had not only high activity (the onset potential of −0.20 V) but also high photoconversion efficiency. In detail, the bandgap of g-C_3N_4 decreased from 2.98 eV to 1.12 eV because of the introduction of boron SAs, leading to the improved absorbance of the visible (VIS) light and infrared (IR) light (Figure 7F). Besides B/g-C_3N_4, the introduction of boron SAs is also efficient to boost the photocatalytic performance of g-CN (B/g-CN), which could activate N_2 and reduce it to NH_3 with a low overpotential of 0.15 V[102] g-C_2N is another import carbon nitride material, and the boron-doped g-C_2N (B/g-C_2N) is also a promising NRR SAC with the theoretical limiting potential of −0.15 V.[87] High catalytic performance has been universally predicted for SACs with boron SAs supported on 2D carbon nitride materials. In addition, extensive density functional theory (DFT) calculations were carried out to investigate the design principles of boron SACs and reveal how the NRR activity and selectivity are affected by the local bonding structure of boron SAs and the boron-substrate charge transfer.[103] By incorporating boron SAs into eight 2D materials, twenty-one models were constructed. Figure 7G shows their free energy changes of the rate-determining step (RDS) of NRR ($\Delta G_{RDS-NRR}$) and HER ($\Delta G_{RDS-HER}$), and smaller $\Delta G_{RDS-NRR}$ occurs when δ gets smaller, whereas $\Delta G_{RDS-HER}$ is relatively positive. This is because the electron transfer from boron SAs to adsorbed N_2 is important for N_2 activation, where more electrons in boron SAs could increase the possibility for such an electron injection, and negatively charged boron SAs could bind the H^+ adatom strongly, leading to high selectivity. The relationship between the catalytic performance toward NRR and the locally chemical environment of boron SAs has been clarified in boron SACs.
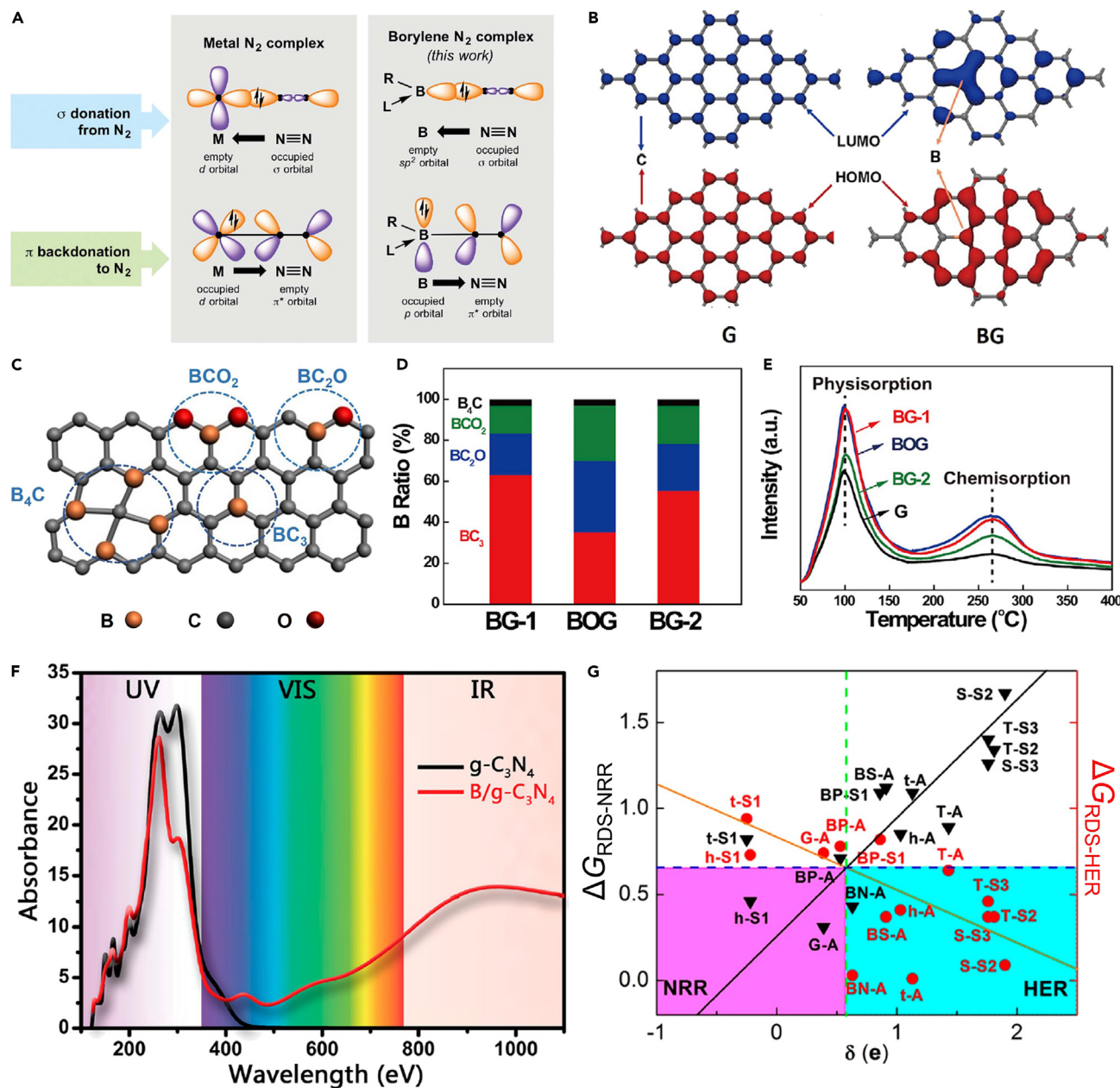
Figure 7. Non-metal SACs with external boron SAs

(A) Schematic illustration of the bonding in well-known end-on-bound transition metal N_2 complexes and prospective application to monovalent boron species. (A) Reproduced with permission.[91] Copyright 2018, American Association for the Advancement of Science.

(B) LUMO (blue) and HOMO (red) of BG and undoped G.

(C) Schematic illustrations of the B_4C, BC_3, BC_2O, and BCO_2 structures.

(D) Percentages of different boron-doped types in BG samples.

(E) N_2 temperature-programmed desorption curves of BG samples and G. (B-E) Reproduced with permission.[92] Copyright 2018, Cell press.

(F) Optical adsorption spectra of g-C_3N_4 (black) and B/g-C_3N_4 (red). (F) Reproduced with permission.[98] Copyright 2018, American Chemical Society.

(G) Computational screening of fourteen catalyst combinations in terms of $\Delta G_{\text{RDS-NRR}}$ and $\Delta G_{\text{RDS-HER}}$ vs. δ.

(G) Reproduced with permission.[103] Copyright 2019, American Chemical Society.

Beside electrocatalytic and photocatalytic NRR, SACs with non-metal SAs were also promising in other reactions. For example, Jiao et al. established the HER activity of graphene-based materials with boron, N, O, P, or S SAs and explored their reactivity origin by combining spectroscopic characterization, electrochemical measurements, and DFT calculations.[86]

SACs WITH INTRINSIC SAs

Beside transition metal atoms, some main-group elements, such as boron and Al, have also been proved to be efficient active sites in SACs. After another decade, at least half of the non-radioactive elements in the periodic table might be fabricated in SACs. However, as aforementioned, the favorable aggregation of external SAs and the limited concentrations of surface vacancy defects make the loading of external SAs relatively low, restricting the further improvement in the catalytic performances of SACs. If the single-atom structure is naturally possessed, high-loading SAs will be expectable.

NOBLE METAL SAs

M_1N_x centers (x = 3 or 4) have been widely confirmed as promising active sites for numbers of thermocatalytic, electrocatalytic, and photocatalytic reactions.[26,104–113] As a class of molecules having natural M_1N_x centers, MTPs are attractive as SACs or SACs precursors. He et al. developed a universal precursor-dilution strategy to synthesize a series of SACs and even bimetallic SACs.[114] Metals tetraphenylporphyrins (M-TPPs), analogous materials of MTP with natural M_1N_4 centers, were co-polymerized with free TPPs, where free TPPs can extend the mean distance between metal atoms dispersed on the as-prepared polymer matrix and thus prevent the aggregation of metal atoms during the subsequent high-temperature pyrolysis. Figure 8A shows the synthesis of the Pt_1N_4-C catalyst using the precursor-dilution strategy with Pt-TPP:TPP = 1:40. Because the first-shell coordination of Pt SAs was unchanged before and after pyrolysis (Figure 8B), the active sites in the Pt_1N_4-C catalyst can be regarded as intrinsic SAs. Several characterization techniques confirmed that Pt is atomically dispersed in carbon matrix with the loading of 0.43 wt %. According to the molar ratio of Pt-TPP:TPP (1:40), the Pt loading should be 0.73 wt %, which suggested the metal loss during preparation. However, without the dilution of free TPPs, Pt atoms aggregated to nanoparticles (Figure 8C). By adjusting the molar ratio of Pt-TPP:TPP, different Pt SAs loadings (0.06, 0.21, 0.43, and 0.73 wt %) can be achieved in Pt_1N_4-C samples. More importantly, with suitable ratios of M-TPP:TPP, Ru_1N_4-C, Rh_1N_4-C, Pd_1N_4-C, In_1N_4-C, Au_1N_4-C, and Ag_1N_4-C can be synthesized; Cd_1N_4-C, Bi_1N_4-C, and Er_1N_4-C that have never been reported can be synthesized; this strategy was effective to synthesis bimetallic SACs with two different precursors, such as Pt-TPP and Sn-TPP to synthesize the Pt_1-Sn_1/N-C catalyst.

As regards MTPs, since the planar tetramer and one-dimensional linear oligomer assembled by individual MTPs molecules were already synthesized,[115,116] 2D MTP sheets are highly expectable (Figure 8D). After forming 2D MTP sheets, the SAs loading can be significantly improved, such as 25.44 wt % for Ru in 2D RuTP sheet. Using DFT calculations, Yao et al. investigated the catalytic performances of thirty 2D MTP sheets toward NRR.[117] Starting with exploring N_2 adsorption (Figure 8E), they found that the end-on adsorption is stronger than the side-on one when metal atoms are in $d^1 \sim d^6$ series but little difference for $d^7 \sim d^{10}$ series. This is because N_2 is always physically adsorbed on these 2D MTP sheets caused by the absence of empty d orbitals for $d^7 \sim d^{10}$ metal atoms. N_2 adsorption on 2D MTP sheets with the metal atoms in $d^2 \sim d^6$ series was relatively strong ($E_{ad-N2} < -0.4$ eV) because of the coexistence of empty and occupied d orbitals. For 2D MTP sheets with d^1 metal atoms, the coordinated N atoms might take away d electrons of metal atoms, and few electrons thus can be back-donated to adsorbed N_2. After computing the free energy profiles of NRR, metal atoms in the three most active 2D MTP sheets were all in $5d$ series, which was attributed to the fact that MN_4 centers with $5d$ metal atoms can transfer electron easier. Besides NRR, 2D MTP sheets have also been explored as SACs toward CO_2RR (Figure 8F),[107] ORR (Figure 8G),[118] etc.[119,120] Utilizing intrinsic SAs achieves not only higher SAs loading but also better activity per specific active site.

NON-NOBLE METAL SAs
MOF-based

Currently, pyrolyzing MOFs are widely used to synthesize carbon-based SACs, and this method is first reported by Yin et al.[33] They prepared a Zn/Co bimetallic MOF with homogeneous distributions of Co^{2+} and Zn^{2+}, forming mixed metal nodes, where Zn^{2+} sites replace Co^{2+} sites and serve as "fences" to expand the adjacent distance between Co^{2+} sites. During the subsequent high-temperature pyrolysis, Zn^{2+} sites were evaporated away because of low boiling point (907°C) and Co^{2+} sites were *it situ* reduced (Figure 9A), forming Co SAC, Co SAs/N-C(800), with Co SAs dispersed on N-doped porous carbon and the Co loading of 1.5 wt %. By increasing the pyrolysis temperature, a higher Co loading (4.3 wt %) was achieved in Co SAs/N-C(900). Co clusters or nanoparticles cannot be observed after careful examination of most areas of the SACs samples. Note that without the introduction of Zn^{2+} sites, Co^{2+} sites preferred to aggregate during
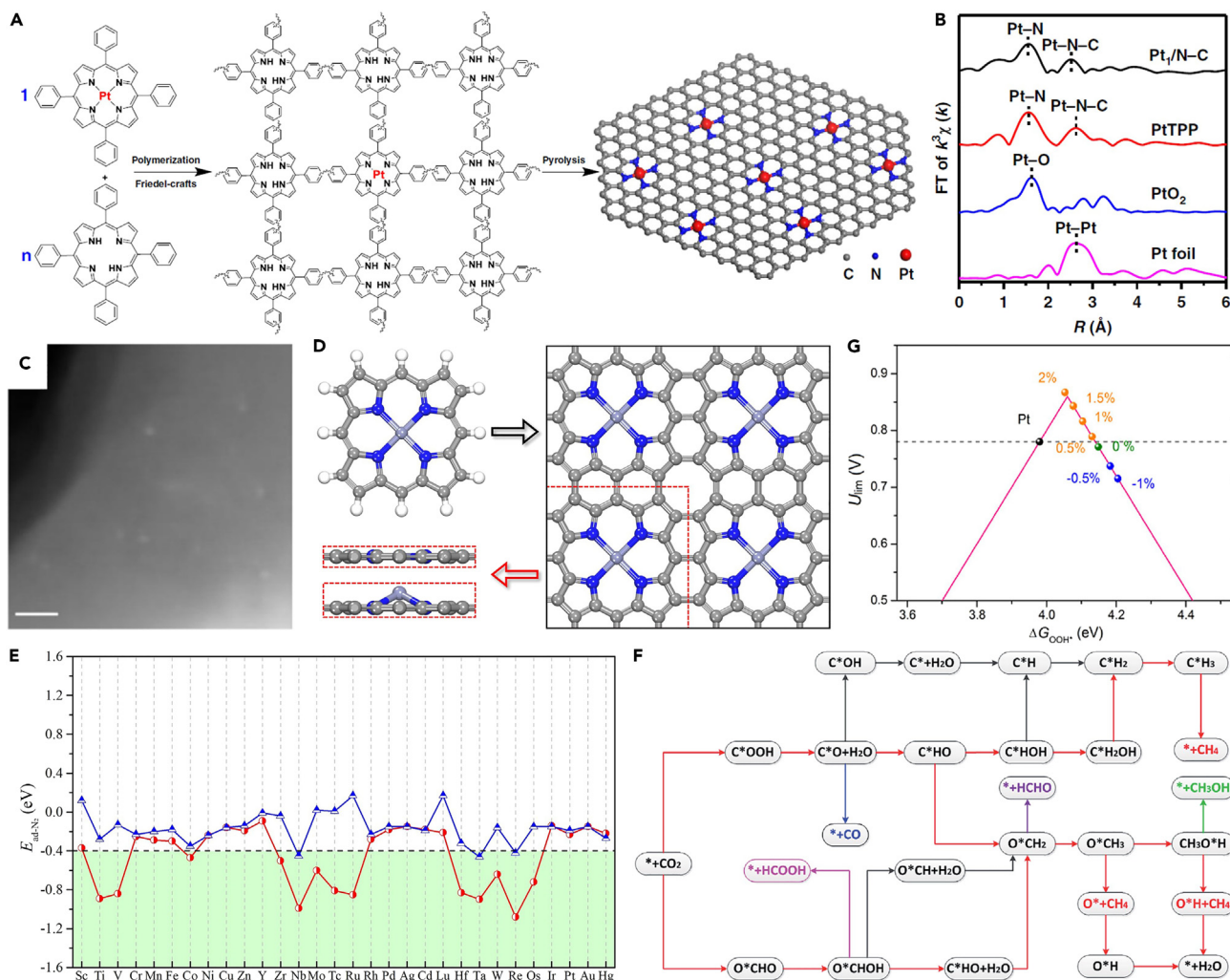
Figure 8. Porphyrin-based SACs with intrinsic SAs

(A) Schematic illustration of the preparation of Pt_1N_4-C catalyst.

(B) The k^3-weighted R-space FT spectra of EXAFS for Pt_1N_4-C, Pt-TPP, PtO_2, and Pt foil.

(C) STEM image of Pt nanoparticles on the polymer matrix with Pt-TPP:TPP = 1:0.

(A–C) Reproduced with permission.[114] Copyright 2019, Nature Publishing Group.

(D) Top views of the optimized MTP molecules and 2D MTP sheets in a 2 × 2 computational supercell.

(E) Adsorption energies of side-on and end-on adsorbed N_2 (E_{ad-N2}) on thirty 2D MTP sheets, where the green area denotes that $E_{ad-N2} < -0.40$ eV.

(D and E) Reproduced with permission.[117] Copyright 2020, Elsevier Inc.

(F) Investigated pathways for CO_2RR on 2D MTP sheets. (F) Reproduced with permission.[107] Copyright 2019, The Royal Society of Chemistry.

(G) Theoretical limiting potential (U_{lim}) as a function of ΔG_{OOH*} with an activity volcano plot on 2D MTP sheet, where the black line denotes Pt (111). (G) Reproduced with permission.[118] Copyright 2017, Elsevier Inc.

pyrolysis, forming Co nanoparticle supported on N-doped carbon. The spatial distribution of Co SAs in the as-prepared Co SAs/N-C catalysts was investigated by analyzing a series of HAADF-STEM images with different focal depths. At specific focal depths, three selected atoms (a_1, b_1, and c_1, Figure 9B) should have different intensities, and the intensity versus defocus function plot indeed indicated that the intensities of three atoms are different (Figure 9C) and c_1 atom located between a_1 and b_1 along the x-axis has the lowest intensity at a focal position along the z axis. Hence, Co SAs were highly dispersed in N-doped carbon, rather than only on the surface. The as-prepared Co SAs/N-C catalysts were more active than the commercial Pt/C catalyst toward ORR in O_2-saturated 0.1 M KOH media, and no obvious decay in activity can be observed even after 5000 continuous cycles. Owing to the high structural adjustability of MOFs, a general strategy to synthesize high-loading and high-performance SACs is provided.
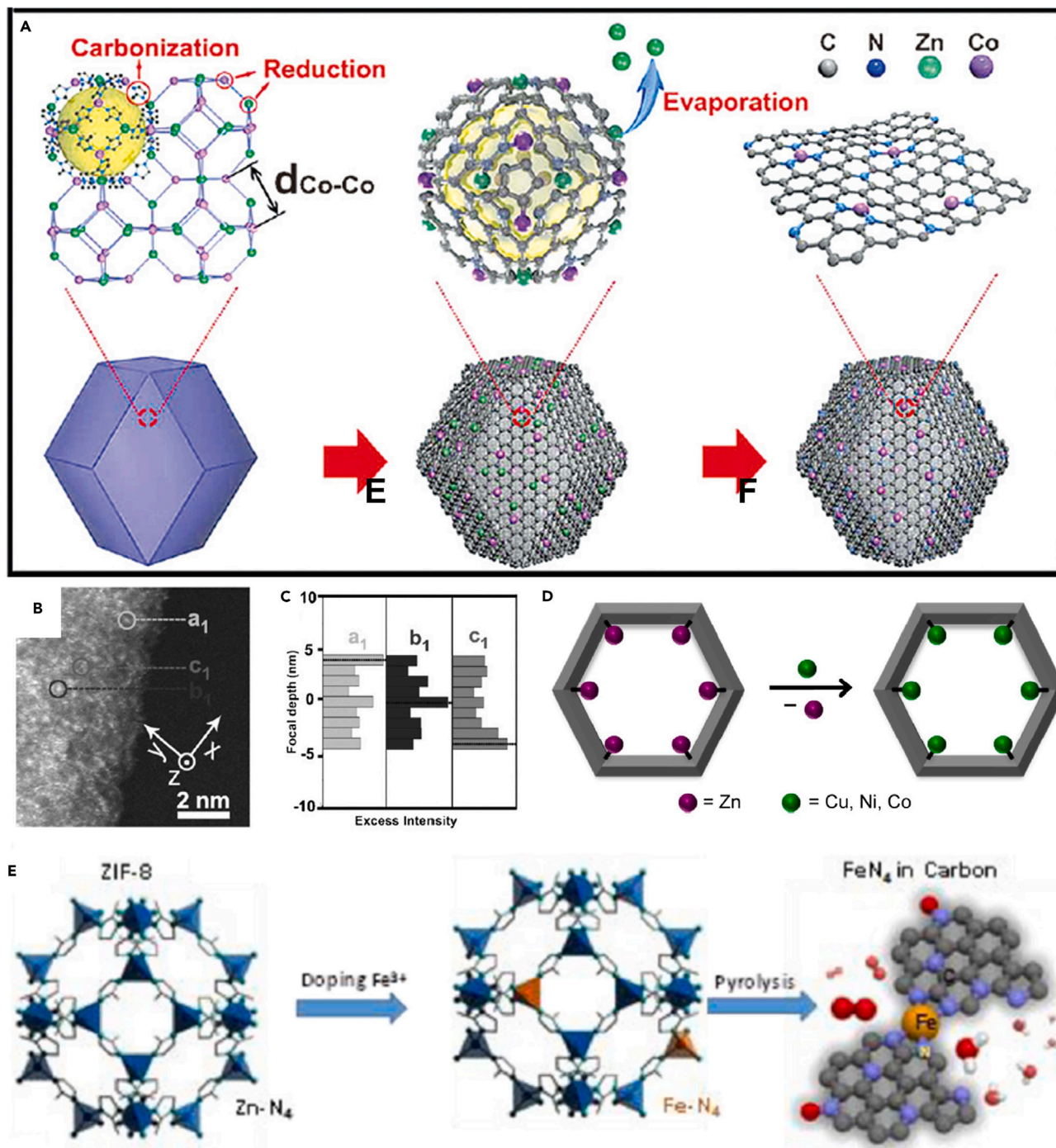
Figure 9. Strategies to synthesize SACs with intrinsic SAs

(A) Schematic illustration of the preparation of Co SAs/N-C catalyst.

(B) Sum of nine aligned HAADF-STEM images of Co SAs/N-C(800).

(C) Excess intensity of a_1, b_1, and c_1 atoms shown in (B).

(A–C) Reproduced with permission.[33] Copyright 2016, Wiley-VCH Verlag GmbH & Co. KGaA, Weinheim.

(D) Schematic illustration of AIM-installed metal atoms undergoing metal exchange. (D) Reproduced with permission.[121] Copyright 2016, American Chemical Society.

(E) Synthesis principles of Fe-doped ZIF-derived catalysts. (E) Reproduced with permission.[122] Copyright 2017, American Chemical Society.

Metal exchange is another efficient approach to fabricate MOFs with mixed metal nodes. Klet et al. successfully installed Cu, Co, and Ni SAs into Zn-MOF by combining the atomic layer deposition in MOFs and metal exchange technique (Figure 9D).[121] After successful metal exchange, the color of Zn-AIM changed from yellow to pale green. The as-prepared precursors held great potential to synthesize SACs with intrinsic Cu, Co, and Ni SAs. Moreover, Zhang et al. simultaneously added Fe and Zn ions with 2-methylimidazole to prepared Fe-doped ZIF-8 containing Zn_1-N_4 and Fe_1-N_4 complexes, and Fe_1N_4 centers were formed by one-step thermal activation with the Fe loading of ~0.5 at% (Figure 9E).[122] The as-prepared Fe SAC achieved respectable ORR activity in challenging acidic media (0.5 M H_2SO_4).

Intrinsic defect-based

Though MTPs/M-TPPs or MOFs are high useful to synthesize SACs with intrinsic SAs, only carbon-based SACs can be prepared. Aiming at broad applications, metal compound-based SACs with intrinsic SAs should be explored. In this regard, intrinsic structural defects with the single-atom structure are attractive, because the concentration of intrinsic defects could be higher than that of single heteroatoms. Regarding high-loading intrinsic defects, 2D materials are promising candidates, because the ultrahigh surface/volume ratio can ensure the exposure of all intrinsic defects to reactants. Beyond graphene, transition metal dichalcogenides (MX_2, X: chalcogen) are another representative family of 2D materials and have been widely used in electronics, electrocatalysis, energy storage and conversion, etc.[123–129] Because the practical physiochemical properties of MX_2 are far behind the theoretical predictions,[130,131] Hong et al. comprehensively investigated the point defects in monolayer MoS_2 samples synthesized by mechanical exfoliation (ME), physical vapor deposition (PVD), and chemical vapor deposition (CVD).[132] Figures 10A–10C summarize the analysis of defects and their concentrations for ten optimally fabricated samples by each method. For PVD samples, antisite defects with one Mo atom replacing one or two S atoms (Mo_S or Mo_{S2}) were dominant defects (Figures 10A and 10C), and vacancies with one or two missing S atoms (V_S or V_{S2}) were frequently observed in ME and CVD samples (Figures 10B and 10C). The concentrations of Mo_S and Mo_{S2} in PVD samples reached 7.0×10^{12} and 2.8×10^{13} cm^{-2}, respectively, and the concentration of V_S in ME and CVD samples was 1.2×10^{13} cm^{-2}. More importantly, antisite M_S and M_{S2} of MX_2 have the single-atom structure with individual under-coordinated metal atoms (Figure 10D) and can be spontaneously formed during PVD, rather than by creating vacancies to capture single heteroatoms (Figure 10E). Hence, they hold great promise to be advanced SACs. Yao et al. theoretically explored the activities of W_S and W_{S2} toward NRR.[133] The density of these defects in Figure 10D was about 6×10^{13} cm^{-2}, which is a practically viable value because an average density of 3×10^{13} cm^{-2} for antisite Mo_{S2} has already been reported for MoS_2.[132] With such a practically viable density, the loadings of W SAs in W_S and W_{S2} are ~4.5 wt %, significantly larger than those of reported SACs with non-carbon supports (usually <2 wt %). Strong N_2 adsorption on W_S can be proved by the partial density of states (PDOS) (Figure 10F), and such a strong interaction activated the adsorbed N_2 by elongating the N-N bond length from 1.108 Å for free N_2 molecule to 1.190 Å. Consequently, W_S can catalyze NRR at a limiting potential of −0.24 V through the enzymatic mechanism, superior than other MX_2-based NRR catalysts, including MX_2-based SACs with external SAs.[103,134,135] The high activity of W_S was ascribed to the movement of the active W atom (W_0) during the reaction, where the movement can be confirmed the PDOS of N_2* on W_S (Figure 10G). Besides high activity, W_S and W_{S2} also exhibited high selectivity, where both H* adsorption (key step for HER) and N_2H_4 formation (side product) are inhibited.

Besides the antisite defects M_S and M_{S2}, the Frenkel defects with interstitial metal atoms of MX_2 can be also regarded as intrinsic SAs.[136] Xu et al. first synthesized pristine MoS_2 monolayer by CVD and then annealed the as-prepared MoS_2 materials in Ar atmosphere at 400°C to fabricate Frenkel-defected MoS_2 (FD-MoS_2, Figure 11A), where FD-MoS_2-3 and FD-MoS_2-5 denote the annealing time of 3 and 5 min, respectively. With increasing annealing time from 3 to 5 min, the average concentration of Frenkel defects increased from 0.50% to 0.85%. The HAADF-STEM image and the atomic model of FD-MoS_2-3 with highlighted Frenkel defected sites are shown in Figures 11B and 11C. It can be seen that Mo atom leaves their own lattice sites and becomes an interstitial anchored by nearby locations, which is consistent with the definition of Frenkel defects. The Frenkel defect also has the single-atom structure with the SAs of the interstitial Mo atoms. FD-MoS_2-3 and FD-MoS_2-5 exhibited superior HER performances compared to pristine MoS_2 and Pt-MoS_2 (a SAC with external Pt SAs on MoS_2) (Figures 11B and 11C), highlighting the Frenkel-defect engineering strategy on 2D materials. Figure 11F is the free energy profile of HER on pristine MoS_2, Pt-MoS_2, and FD-MoS_2, and the Frenkel defect had the optimal free energy of H* adsorption (close to 0 eV). This experimental work strongly supports the feasibility of metal compound-based SACs with intrinsic SAs.
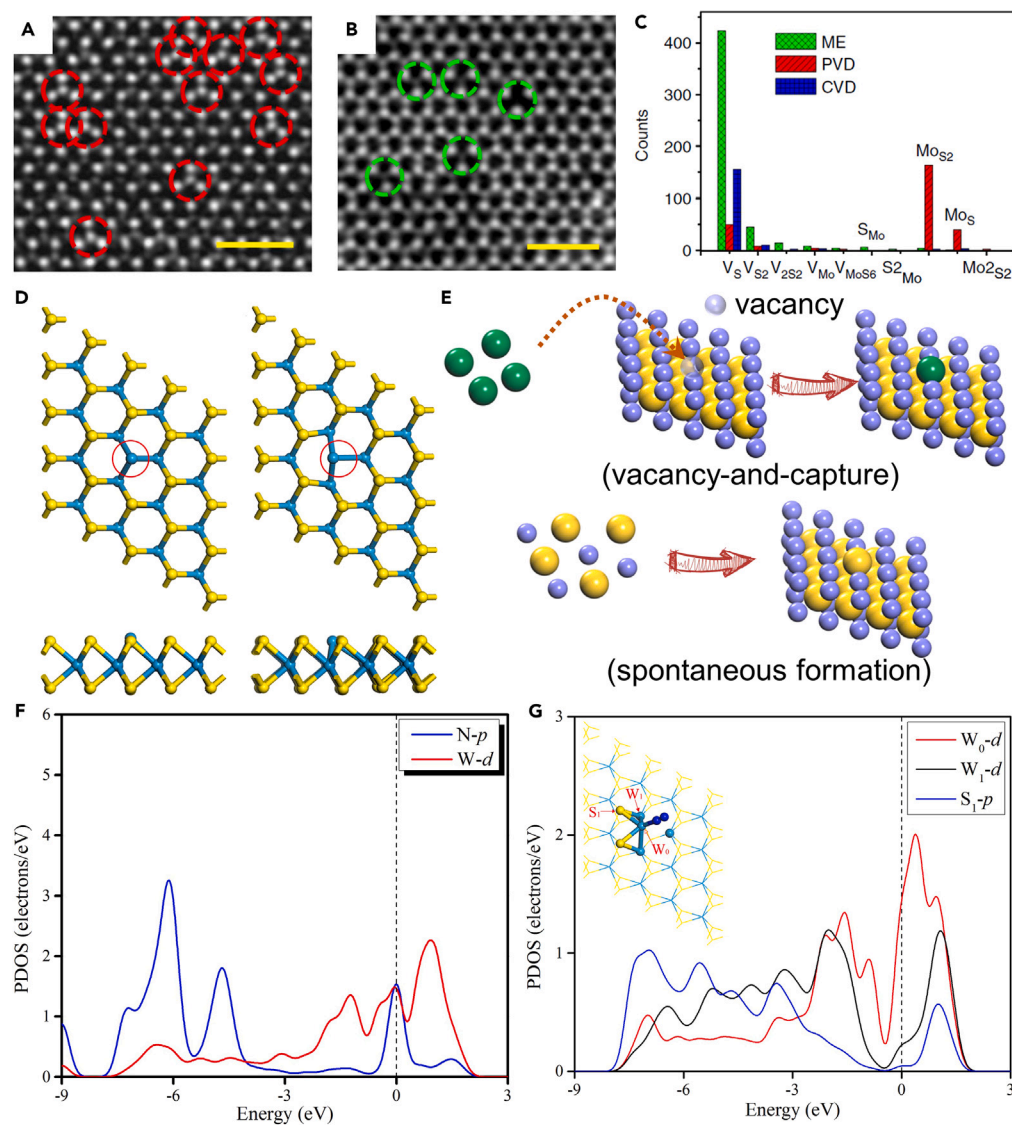
Figure 10. Antisite defect-based SACs with intrinsic Mo SAs

(A and B) STEM images for antisite defects in a PVD sample (A) and vacancy defects in an ME sample (B). The case of CVD samples is similar to (B).

(C) Counts of various point defects in PVD, CVD, and ME samples.

(A–C) Reproduced with permission.[132] Copyright 2015, Nature Publishing Group.

(D) Optimized structures of antisite W_S and W_{S2}.

(D) Reproduced with permission.[133] Copyright 2019, The Royal Society of Chemistry.

(E) Scheme of the vacancy-and-capture formation of MX_2-based SACs with external SAs and the spontaneous formation of the single-atom structure of antisite M_S in MX_2.

(F and G) PDOS of side-on-adsorbed N_2^* (F) and end-on-adsorbed N_2^* (G) on W_S. (F–G) Reproduced with permission.[133] Copyright 2019, The Royal Society of Chemistry.

PERSPECTIVES AND CHALLENGES

SACs have evolved to be a research frontier in thermocatalysis, electrocatalysis, and photocatalysis. The unique atomic structure enables every active site works efficiently, making SACs highly promising. Moreover, the active sites of SACs are well-defined, a tremendous advance in the field of heterogeneous catalysts, and the structure-activity relationship thus can be comprehensively understood and subsequently exploited in the rational design of high-performance SACs. Though numerous progress have been made in recent years, the breakthrough or the commercialization of SACs is still limited by the
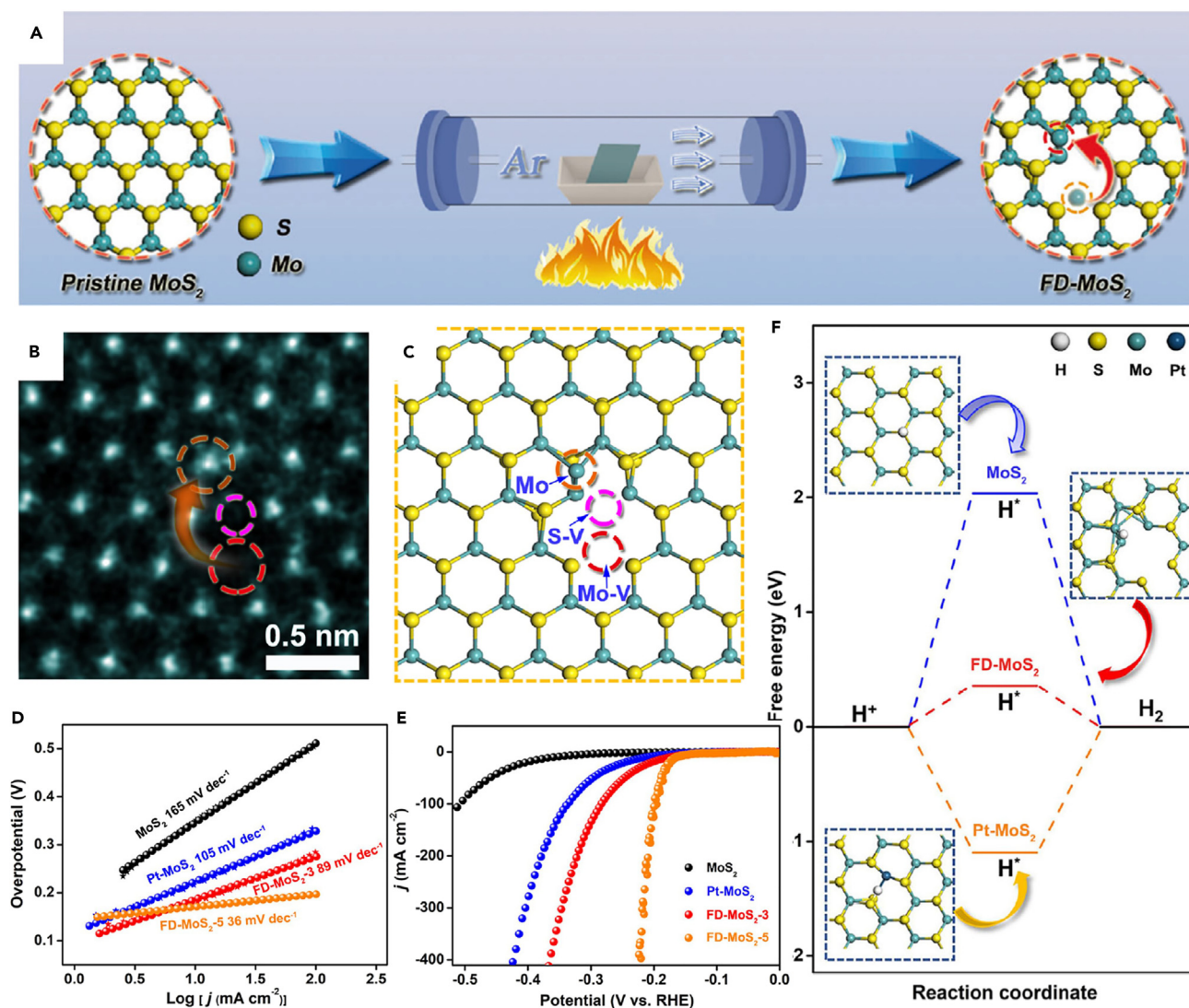
Figure 11. Frenkel defect-based SACs with intrinsic Mo SAs
(A) Schematic synthetic procedure for FD-MoS$_2$.
(B and C) Atomic-resolution HAADF-STEM image (B) and atomic structure (C) of FD-MoS$_2$.
(D and E) Polarization curves (D) and Tafel plots (E) of pristine MoS$_2$, Pt-MoS$_2$, FD-MoS$_2$-3, and FD-MoS$_2$-5 in 0.5 M H$_2$SO$_4$.
(F) Free energy profile of HER on pristine MoS$_2$, Pt-MoS$_2$, and FD-MoS$_2$, including the top views of H*.
(A–F) Reproduced with permission.[136] Copyright 2022, Nature Publishing Group.

relatively low SAs loading because of the favorable aggregation of external SAs. To circumvent this inartificial limitation to obtain high-loading SACs, fabricating SACs with intrinsic SAs is of great worth and necessity. However, further development of SACs with high-loading intrinsic SAs for advancing the practical implementation is still challenging.

Currently the number of experimental studies regarding SACs with intrinsic SAs is negligible compared to that of SACs with external SAs, and future theoretical studies regarding intrinsic SAs thus should focus on (1) higher experimental feasibility: High-loading intrinsic SAs are indeed naturally owned by some systems, such as 2D MTP sheets,[107,117–120] but the corresponding experimental synthesis is of great difficulty. Predicted performances based on SACs systems with higher experimental feasibility, such as 2D M-HAB sheet with the single-metal nodes and the ligand of hexaaminobenzene,[137] will be more attractive for experimentalists, providing them practically meaningful evidence and guidance; (2) higher catalytic performance: The predicted performances of the aforementioned SACs with intrinsic SAs are not excellent

enough.[107,117–120,133] High-throughput techniques and ML should be utilized to make highly efficient screening for thousands of candidates and thereby achieve higher performance; (3) higher stability: A common concern for SACs is the stability under harsh reaction conditions, where SAs, the ligand of SAs, and even the substrate might greatly vary, leading to activity decay. Though the thermodynamic and kinetic stabilities of the aforementioned SACs with intrinsic SAs have been theoretically confirmed,[107,117–120,133] their stabilities under harsh reaction conditions are still doubtful. More complex theoretical simulations, such as the diverse implicit/explicit solvation models, the computational Pourbaix diagrams, and even molecule dynamics, should be conducted to provide stronger evidence for SACs durability.

On the other hand, future experimental studies regarding intrinsic SAs should focus on: (1) higher SAs loading/density: The loading/density of intrinsic SAs can indeed exceed that of external SAs, but is still low compared to the whole surface. More advances in experiments are required. For example, increasing the density of antisite defects by optimizing the chemical potential of the corresponding transition metal; increasing the fraction of exchanged metal nodes in MOFs by optimizing the experimental conditions; (2) advanced characterization and detection techniques: In situ and operando spectroscopies should be well used to explore (i) the real active sites, (ii) the reaction intermediates, (iii) the variation in the coordination environment/valence state of intrinsic SAs, and (iv) the activity decay behavior of SACs, which could in turn provide guidance for theoretical research.

DECLARATION OF INTERESTS

The authors declare no competing interests.

REFERENCES

1. Le Page, A.J. (1987). Applied Heterogeneous Catalysis (Editions Technip).

2. Schlögl, R. (2015). Heterogeneous Catalysis. Angew. Chen. Int. Ed. 54, 3465–3520. https://doi.org/10.1002/anie.201410738.

3. MacFarlane, D.R., Cherepanov, P.V., Choi, J., Suryanto, B.H., Hodgetts, R.Y., Bakker, J.M., Ferrero Vallana, F.M., and Simonov, A.N. (2020). A Roadmap to the Ammonia Economy. Joule 4, 1186–1205. https://doi.org/10.1016/j.joule.2020.04.004.

4. Resasco, J., Abild-Pedersen, F., Hahn, C., Bao, Z., Koper, M.T.M., and Jaramillo, T.F. (2022). Enhancing the Connection between Computation and Experiments in Electrocatalysis. Nat. Catal. 5, 374–381. https://doi.org/10.1038/s41929-022-00789-0.

5. Lee, J.S., Tai Kim, S., Cao, R., Choi, N.S., Liu, M., Lee, K.T., and Cho, J. (2011). Metal–Air Batteries with High Energy Density: Li–Air Versus Zn–Air. Adv. Energy Mater. 1, 34–50. https://doi.org/10.1002/aenm.201000010.

6. Munnik, P., de Jongh, P.E., and de Jong, K.P. (2015). Recent Developments in the Synthesis of Supported Catalysts. Chem. Rev. 115, 6687–6718. https://doi.org/10.1021/cr500486u.

7. Zhang, J., Wang, L., Zhang, B., Zhao, H., Kolb, U., Zhu, Y., Liu, L., Han, Y., Wang, G., Wang, C., et al. (2018). Sinter-Resistant Metal Nanoparticle Catalysts Achieved by Immobilization within Zeolite Crystals Via Seed-Directed Growth. Nat. Catal. 1, 540–546. https://doi.org/10.1038/s41929-018-0098-1.

8. Campelo, J.M., Luna, D., Luque, R., Marinas, J.M., and Romero, A.A. (2009). Sustainable Preparation of Supported Metal Nanoparticles and Their Applications in Catalysis. ChemSusChem 2, 18–45. https://doi.org/10.1002/cssc.200800227.

9. Herzing, A.A., Kiely, C.J., Carley, A.F., Landon, P., and Hutchings, G.J. (2008). Identification of Active Gold Nanoclusters on Iron Oxide Supports for CO Oxidation. Science 321, 1331–1335. https://doi.org/10.1126/science.1159639.

10. Xu, Z., Xiao, F.S., Purnell, S.K., Alexeev, O., Kawi, S., Deutsch, S.E., and Gates, B.C. (1994). Size-Dependent Catalytic Activity of Supported Metal Clusters. Nature 372, 346–348. https://doi.org/10.1038/372346a0.

11. Corma, A., Concepción, P., Boronat, M., Sabater, M.J., Navas, J., Yacaman, M.J., Larios, E., Posadas, A., López-Quintela, M.A., Buceta, D., et al. (2013). Exceptional Oxidation Activity with Size-Controlled Supported Gold Clusters of Low Atomicity. Nat. Chem. 5, 775–781. https://doi.org/10.1038/nchem.1721.

12. Yang, X.F., Wang, A., Qiao, B., Li, J., Liu, J., and Zhang, T. (2013). Single-Atom Catalysts: A New Frontier in Heterogeneous Catalysis. Acc. Chem. Res. 46, 1740–1748. https://doi.org/10.1021/ar300361m.

13. Wu, G., More, K.L., Johnston, C.M., and Zelenay, P. (2011). High-Performance Electrocatalysts for Oxygen Reduction Derived from Polyaniline, Iron, and Cobalt. Science 332, 443–447. https://doi.org/10.1126/science.1200832.

14. Qiao, B., Wang, A., Yang, X., Allard, L.F., Jiang, Z., Cui, Y., Liu, J., Li, J., and Zhang, T. (2011). Single-Atom Catalysis of CO Oxidation Using Pt1/FeOx. Nat. Chem. 3, 634–641. https://doi.org/10.1038/nchem.1095.

15. Xie, F., Cui, X., Zhi, X., Yao, D., Johannessen, B., Lin, T., Tang, J., Woodfield, T.B.F., Gu, L., and Qiao, S.Z. (2023). A General Approach to 3D-Printed Single-Atom Catalysts. Nat. Synth. 2, 129–139. https://doi.org/10.1038/s44160-022-00193-3.

16. Han, G.F., Li, F., Rykov, A.I., Im, Y.K., Yu, S.Y., Jeon, J.P., Kim, S.J., Zhou, W., Ge, R., Ao, Z., et al. (2022). Abrading Bulk Metal into Single Atoms. Nat. Nanotechnol. 17, 403–407. https://doi.org/10.1038/s41565-022-01075-7.

17. Daelman, N., Capdevila-Cortada, M., and López, N. (2019). Dynamic Charge and Oxidation State of Pt/CeO2 Single-Atom Catalysts. Nat. Mater. 18, 1215–1221. https://doi.org/10.1038/s41563-019-0444-y.

18. Xu, H., Cheng, D., Cao, D., and Zeng, X.C. (2018). A Universal Principle for a Rational Design of Single-Atom Electrocatalysts. Nat. Catal. 1, 339–348. https://doi.org/10.1038/s41929-018-0063-z.

19. Xu, H., Liu, E., Xie, J., Smyth, R.L., Zhou, Q., Zhao, R., Zang, N., Long, X., Tang, Y., Estill, J., et al. (2020). Highly Selective Electrocatalytic CO2 Reduction to Ethanol by Metallic Clusters Dynamically Formed from Atomically Dispersed Copper. Nat. Energy 8, 623–632. https://doi.org/10.1038/s41560-020-0666-x.

20. Chen, Z.W., Lu, Z., Chen, L.X., Jiang, M., Chen, D., and Singh, C.V. (2021). Machine-Learning-Accelerated Discovery of Single-Atom Catalysts Based on Bidirectional Activation Mechanism. Chem Catal. 1, 183–195. https://doi.org/10.1016/j.checat.2021.03.003.

21. Lee, B.H., Park, S., Kim, M., Sinha, A.K., Lee, S.C., Jung, E., Chang, W.J., Lee, K.S., Kim, J.H., Cho, S.P., et al. (2019). Reversible and Cooperative Photoactivation of Single-Atom Cu/TiO2 Photocatalysts. Nat. Mater. 18, 620–626. https://doi.org/10.1038/s41563-019-0344-1.

22. Han, L., Song, S., Liu, M., Yao, S., Liang, Z., Cheng, H., Ren, Z., Liu, W., Lin, R., Qi, G., et al. (2020). Stable and Efficient Single-Atom Zn Catalyst for CO2 Reduction to CH4. J. Am. Chem. Soc. 142, 12563–12567. https://doi.org/10.1021/jacs.9b12111.

23. Chen, Z.W., Yan, J.M., and Jiang, Q. (2019). Single or Double: Which Is the Altar of Atomic Catalysts for Nitrogen Reduction Reaction? Small Methods 3, 1800291. https://doi.org/10.1002/smtd.201800291.

24. Cao, L., Liu, W., Luo, Q., Yin, R., Wang, B., Weissenrieder, J., Soldemo, M., Yan, H., Lin, Y., Sun, Z., et al. (2019). Atomically Dispersed Iron Hydroxide Anchored on Pt for Preferential Oxidation of CO in H2. Nature 565, 631–635. https://doi.org/10.1038/s41586-018-0869-5.

25. Kong, N., Fan, X., Liu, F., Wang, L., Lin, H., Li, Y., and Lee, S.T. (2020). Single Vanadium Atoms Anchored on Graphitic Carbon Nitride as a High-Performance Catalyst for Non-Oxidative Propane Dehydrogenation. ACS Nano 14, 5772–5779. https://doi.org/10.1021/acsnano.0c00659.

26. Xiong, Y., Dong, J., Huang, Z.Q., Xin, P., Chen, W., Wang, Y., Li, Z., Jin, Z., Xing, W., Zhuang, Z., et al. (2020). Single-Atom Rh/N-Doped Carbon Electrocatalyst for Formic Acid Oxidation. Nat. Nanotechnol. 15, 390–397. https://doi.org/10.1038/s41565-020-0665-x.

27. Maurer, F., Jelic, J., Wang, J., Gänzler, A., Dolcet, P., Wöll, C., Wang, Y., Studt, F., Casapu, M., and Grunwaldt, J.D. (2020). Tracking the Formation, Fate and Consequence for Catalytic Activity of Pt Single Sites on CeO2. Nat. Catal. 3, 824–833. https://doi.org/10.1038/s41929-020-00508-7.

28. Wei, S., Li, A., Liu, J.C., Li, Z., Chen, W., Gong, Y., Zhang, Q., Cheong, W.C., Wang, Y., Zheng, L., et al. (2018). Direct Observation of Noble Metal Nanoparticles Transforming to Thermally Stable Single Atoms. Nat. Nanotechnol. 13, 856–861. https://doi.org/10.1038/s41565-018-0197-9.

29. Hannagan, R.T., Giannakakis, G., Réocreux, R., Schumann, J., Finzel, J., Wang, Y., Michaelides, A., Deshlahra, P., Christopher, P., Flytzani-Stephanopoulos, M., et al. (2021). First-Principles Design of a Single-Atom–Alloy Propane Dehydrogenation Catalyst. Science 372, 1444–1447. https://doi.org/10.1126/science.abg838.

30. Vijay, S., Ju, W., Brückner, S., Tsang, S.C., Strasser, P., and Chan, K. (2021). Unified Mechanistic Understanding of CO2 Reduction to CO on Transition Metal and Single Atom Catalysts. Nat. Catal. 4, 1024–1031. https://doi.org/10.1038/s41929-021-00705-y.

31. Li, H., Wang, L., Dai, Y., Pu, Z., Lao, Z., Chen, Y., Wang, M., Zheng, X., Zhu, J., Zhang, W., et al. (2018). Synergetic Interaction between Neighbouring Platinum Monomers in CO2 Hydrogenation. Nat. Nanotechnol. 13, 411–417. https://doi.org/10.1038/s41565-018-0089-z.

32. Yao, Y., Huang, Z., Xie, P., Wu, L., Ma, L., Li, T., Pang, Z., Jiao, M., Liang, Z., Gao, J., et al. (2019). High Temperature Shockwave Stabilized Single Atoms. Nat. Nanotechnol. 14, 851–857. https://doi.org/10.1038/s41565-019-0518-7.

33. Yin, P., Yao, T., Wu, Y., Zheng, L., Lin, Y., Liu, W., Ju, H., Zhu, J., Hong, X., Deng, Z., et al. (2016). Single Cobalt Atoms with Precise N-Coordination as Superior Oxygen Reduction Reaction Catalysts. Angew. Chem. Int. Ed. 128, 10958–10963. https://doi.org/10.1002/ange.201604802.

34. Zhao, C., Dai, X., Yao, T., Chen, W., Wang, X., Wang, J., Yang, J., Wei, S., Wu, Y., and Li, Y. (2017). Ionic Exchange of Metal–Organic Frameworks to Access Single Nickel Sites for Efficient Electroreduction of CO2. J. Am. Chem. Soc. 139, 8078–8081. https://doi.org/10.1021/jacs.7b02736.

35. Song, Z., Zhang, L., Doyle-Davis, K., Fu, X., Luo, J.L., and Sun, X. (2020). Recent Advances in MOF-Derived Single Atom Catalysts for Electrochemical Applications. Adv. Energy Mater. 10, 2001561. https://doi.org/10.1002/aenm.202001561.

36. Chen, Y., Ji, S., Wang, Y., Dong, J., Chen, W., Li, Z., Shen, R., Zheng, L., Zhuang, Z., Wang, D., and Li, Y. (2017). Isolated Single Iron Atoms Anchored on N-Doped Porous Carbon as an Efficient Electrocatalyst for the Oxygen Reduction Reaction. Angew. Chem. Int. Ed. 56, 6937–6941. https://doi.org/10.1002/anie.201702473.

37. Geng, Z., Liu, Y., Kong, X., Li, P., Li, K., Liu, Z., Du, J., Shu, M., Si, R., and Zeng, J. (2018). Achieving a Record-High Yield Rate of 120.9 Mugnh3 Mgcat.-1 H-1 for N2 Electrochemical Reduction over Ru Single-Atom Catalysts. Adv. Mater. 30, 1803498. https://doi.org/10.1002/adma.201803498.

38. Gu, J., Hsu, C.S., Bai, L., Chen, H.M., and Hu, X. (2019). Atomically Dispersed Fe(3+) Sites Catalyze Efficient CO2 Electroreduction to CO. Science 364, 1091–1094. https://doi.org/10.1126/science.aaw751.

39. Zhang, L., Zhou, H., Yang, X., Zhang, S., Zhang, H., Yang, X., Su, X., Zhang, J., and Lin, Z. (2023). Boosting Electroreduction Kinetics of Nitrogen to Ammonia Via Atomically Dispersed Sn Protuberance. Angew. Chem. Int. Ed. 62, 202217473. https://doi.org/10.1002/anie.202217473.

40. Zhuo, H.Y., Zhang, X., Liang, J.X., Yu, Q., Xiao, H., and Li, J. (2020). Theoretical Understandings of Graphene-Based Metal Single-Atom Catalysts: Stability and Catalytic Performance. Chem. Rev. 120, 12315–12341. https://doi.org/10.1021/acs.chemrev.0c00818.

41. Wang, A., Li, J., and Zhang, T. (2018). Heterogeneous Single-Atom Catalysis. Nat. Rev. Chem 2, 65–81. https://doi.org/10.1038/s41570-018-0010-1.

42. Wang, Y., Mao, J., Meng, X., Yu, L., Deng, D., and Bao, X. (2019). Catalysis with Two-Dimensional Materials Confining Single Atoms: Concept, Design, and Applications. Chem. Rev. 119, 1806–1854. https://doi.org/10.1021/acs.chemrev.8b00501.

43. Li, L., Chang, X., Lin, X., Zhao, Z.J., and Gong, J. (2020). Theoretical Insights into Single-Atom Catalysts. Chem. Soc. Rev. 49, 8156–8178. https://doi.org/10.1039/D0CS00795A.

44. Chen, Y., Ji, S., Chen, C., Peng, Q., Wang, D., and Li, Y. (2018). Single-Atom Catalysts: Synthetic Strategies and Electrochemical Applications. Joule 2, 1242–1264. https://doi.org/10.1016/j.joule.2018.06.019.

45. Lang, R., Du, X., Huang, Y., Jiang, X., Zhang, Q., Guo, Y., Liu, K., Qiao, B., Wang, A., and Zhang, T. (2020). Single-Atom Catalysts Based on the Metal–Oxide Interaction. Chem. Rev. 120, 11986–12043. https://doi.org/10.1021/acs.chemrev.0c00797.

46. Kaiser, S.K., Chen, Z., Faust Akl, D., Mitchell, S., and Pérez-Ramírez, J. (2020). Single-Atom Catalysts across the Periodic Table. Chem. Rev. 120, 11703–11809. https://doi.org/10.1021/acs.chemrev.0c00576.

47. Ding, S., Hülsey, M.J., Pérez-Ramírez, J., and Yan, N. (2019). Transforming Energy with Single-Atom Catalysts. Joule 3, 2897–2929. https://doi.org/10.1016/j.joule.2019.09.015.

48. Beniya, A., and Higashi, S. (2019). Towards Dense Single-Atom Catalysts for Future Automotive Applications. Nat. Catal. 2, 590–602. https://doi.org/10.1038/s41929-019-0282-y.

49. Lin, L., Zhou, W., Gao, R., Yao, S., Zhang, X., Xu, W., Zheng, S., Jiang, Z., Yu, Q., Li, Y.W., et al. (2017). Low-Temperature Hydrogen Production from Water and Methanol Using Pt/Alpha-MoC Catalysts. Nature 544, 80–83. https://doi.org/10.1038/nature21672.

50. Cheng, N., Stambula, S., Wang, D., Banis, M.N., Liu, J., Riese, A., Xiao, B., Li, R., Sham, T.K., Liu, L.M., et al. (2016). Platinum Single-Atom and Cluster Catalysis of the Hydrogen Evolution Reaction. Nat. Commun. 7, 13638. https://doi.org/10.1038/ncomms13638.

51. Liu, G., Robertson, A.W., Li, M.M.J., Kuo, W.C.H., Darby, M.T., Muhieddine, M.H., Lin, Y.C., Suenaga, K., Stamatakis, M., Warner, J.H., and Tsang, S.C.E. (2017). MoS2 Monolayer Catalyst Doped with Isolated Co Atoms for the Hydrodeoxygenation Reaction. Nat. Chem. 9, 810–816. https://doi.org/10.1038/nchem.2740.

52. Li, M., Zhao, Z., Cheng, T., Fortunelli, A., Chen, C.Y., Yu, R., Zhang, Q., Gu, L., Merinov, B.V., Lin, Z., et al. (2016). Ultrafine Jagged Platinum Nanowires Enable Ultrahigh Mass Activity for the Oxygen Reduction Reaction. Science 354, 1414–1419. https://doi.org/10.1126/science.aaf9050.

53. Yang, N., Cheng, H., Liu, X., Yun, Q., Chen, Y., Li, B., Chen, B., Zhang, Z., Chen, X., Lu, Q., et al. (2018). Amorphous/Crystalline Hetero-Phase Pd Nanosheets: One-Pot Synthesis and Highly Selective Hydrogenation Reaction. Adv. Mater. 30, 1803234. https://doi.org/10.1002/adma.201803234.

54. Zhang, F., Zhu, Y., Lin, Q., Zhang, L., Zhang, X., and Wang, H. (2021). Noble-Metal Single-Atoms in Thermocatalysis, Electrocatalysis, and Photocatalysis. Energy Environ. Sci. 14, 2954–3009. https://doi.org/10.1039/D1EE00247C.

55. Li, M., Duanmu, K., Wan, C., Cheng, T., Zhang, L., Dai, S., Chen, W., Zhao, Z., Li, P., Fei, H., et al. (2019). Single-Atom Tailoring of Platinum Nanocatalysts for High-Performance Multifunctional Electrocatalysis. Nat. Catal. 2, 495–503. https://doi.org/10.1038/s41929-019-0279-6.

56. Lin, J., Wang, A., Qiao, B., Liu, X., Yang, X., Wang, X., Liang, J., Li, J., Liu, J., and Zhang, T. (2013). Remarkable Performance of Ir1/FeOx Single-Atom Catalyst in Water Gas Shift Reaction. J. Am. Chem. Soc. 135, 15314–15317. https://doi.org/10.1021/ja408574m.

57. Wei, H., Liu, X., Wang, A., Zhang, L., Qiao, B., Yang, X., Huang, Y., Miao, S., Liu, J., and Zhang, T. (2014). FeOx-Supported Platinum Single-Atom and Pseudo-Single-Atom Catalysts for Chemoselective Hydrogenation of Functionalized Nitroarenes. Nat. Commun. 5, 5634. https://doi.org/10.1038/ncomms6634.

58. Du, P., Qi, R., Zhang, Y., Gu, Q., Xu, X., Tan, Y., Liu, X., Wang, A., Zhu, B., Yang, B., and Zhang, T. (2022). Single-Atom-Driven Dynamic Carburization over Pd1–FeOx Catalyst Boosting CO2 Conversion. Chem 8, 3252–3262. https://doi.org/10.1016/j.chempr.2022.08.012.

59. Li, L., Wang, A., Qiao, B., Lin, J., Huang, Y., Wang, X., and Zhang, T. (2013). Origin of the High Activity of Au/Feox for Low-Temperature Co Oxidation: Direct Evidence for a Redox Mechanism. J. Catal. 299, 90–100. https://doi.org/10.1016/j.jcat.2012.11.019.

60. Sun, L., Cao, L., Su, Y., Wang, C., Lin, J., and Wang, X. (2022). Ru1/FeOx Single-Atom Catalyst with Dual Active Sites for Water Gas Shift Reaction without Methanation. Appl. Catal., B 318, 121841. https://doi.org/10.1016/j.apcatb.2022.121841.

61. Lin, J., Qiao, B., Li, N., Li, L., Sun, X., Liu, J., Wang, X., and Zhang, T. (2015). Little Do More: A Highly Effective Pt1/FeOx Single-Atom Catalyst for the Reduction of NO by H2. Chem. Commun. 51, 7911–7914. https://doi.org/10.1039/C5CC00714C.

62. Wei, H., Ren, Y., Wang, A., Liu, X., Liu, X., Zhang, L., Miao, S., Li, L., Liu, J., Wang, J., et al. (2017). Remarkable Effect of Alkalis on the Chemoselective Hydrogenation of Functionalized Nitroarenes over High-Loading Pt/FeOx Catalysts. Chem. Sci. 8, 5126–5131. https://doi.org/10.1039/C7SC00568G.

63. Sadykov, I.I., Zabilskiy, M., Clark, A.H., Krumeich, F., Sushkevich, V., van Bokhoven, J.A., Nachtegaal, M., and Safonova, O.V. (2021). Time-Resolved Xas Provides Direct Evidence for Oxygen Activation on Cationic Iron in a Bimetallic Pt-FeOx/Al2O3 Catalyst. ACS Catal. 11, 11793–11805. https://doi.org/10.1021/acscatal.1c02795.

64. Ding, K., Gulec, A., Johnson, A.M., Schweitzer, N.M., Stucky, G.D., Marks, L.D., and Stair, P.C. (2015). Identification of Active Sites in CO Oxidation and Water-Gas Shift over Supported Pt Catalysts. Science 350, 189–192. https://doi.org/10.1126/science.aac6368.

65. Yang, M., Li, S., Wang, Y., Herron, J.A., Xu, Y., Allard, L.F., Lee, S., Huang, J., Mavrikakis, M., and Flytzani-Stephanopoulos, M. (2014). Catalytically Active Au-O (Oh) X-Species Stabilized by Alkali Ions on Zeolites and Mesoporous Oxides. Science 346, 1498–1501. https://doi.org/10.1126/science.1260526.

66. Vilé, G., Albani, D., Nachtegaal, M., Chen, Z., Dontsova, D., Antonietti, M., López, N., and Pérez-Ramírez, J. (2015). A Stable Single-Site Palladium Catalyst for Hydrogenations. Angew. Chem. Int. Ed. 54, 11265–11269. https://doi.org/10.1002/anie.201505073.

67. Peterson, E.J., DeLaRiva, A.T., Lin, S., Johnson, R.S., Guo, H., Miller, J.T., Hun Kwak, J., Peden, C.H.F., Kiefer, B., Allard, L.F., et al. (2014). Low-Temperature Carbon Monoxide Oxidation Catalysed by Regenerable Atomically Dispersed Palladium on Alumina. Nat. Commun. 5, 4885–4911. https://doi.org/10.1038/ncomms5885.

68. Thomas, J.M. (2015). Tens of Thousands of Atoms Replaced by One. Nature 525, 325–326. https://doi.org/10.1038/525325a.

69. Liu, P., Zhao, Y., Qin, R., Mo, S., Chen, G., Gu, L., Chevrier, D.M., Zhang, P., Guo, Q., Zang, D., et al. (2016). Photochemical Route for Synthesizing Atomically Dispersed Palladium Catalysts. Science 352, 797–801. https://doi.org/10.1126/science.aaf5251.

70. Han, B., Guo, Y., Huang, Y., Xi, W., Xu, J., Luo, J., Qi, H., Ren, Y., Liu, X., Qiao, B., and Zhang, T. (2020). Strong Metal–Support Interactions between Pt Single Atoms and TiO2. Angew. Chem. Int. Ed. 59, 11824–11829. https://doi.org/10.1002/anie.202003208.

71. Guo, Y., Huang, Y., Zeng, B., Han, B., Akri, M., Shi, M., Zhao, Y., Li, Q., Su, Y., Li, L., et al. (2022). Photo-Thermo Semi-Hydrogenation of Acetylene on Pd1/TiO2 Single-Atom Catalyst. Nat. Commun. 13, 2648. https://doi.org/10.1038/s41467-022-30291-x.

72. Tang, Y., Asokan, C., Xu, M., Graham, G.W., Pan, X., Christopher, P., Li, J., and Sautet, P. (2019). Rh Single Atoms on TiO2 Dynamically Respond to Reaction Conditions by Adapting Their Site. Nat. Commun. 10, 4488. https://doi.org/10.1038/s41467-019-12461-6.

73. Thang, H.V., Pacchioni, G., DeRita, L., and Christopher, P. (2018). Nature of Stable Single Atom Pt Catalysts Dispersed on Anatase TiO2. J. Catal. 367, 104–114. https://doi.org/10.1016/j.jcat.2018.08.025.

74. Humphreys, J., Lan, R., and Tao, S. (2021). Development and Recent Progress on Ammonia Synthesis Catalysts for Haber–Bosch Process. Adv. Energy Sustain. Res. 2, 2000043. https://doi.org/10.1002/aesr.202000043.

75. Erisman, J.W., Sutton, M.A., Galloway, J., Klimont, Z., and Winiwarter, W. (2008). How a Century of Ammonia Synthesis Changed the World. Nat. Geosci. 1, 636–639. https://doi.org/10.1038/ngeo325.

76. Foster, S.L., Bakovic, S.I.P., Duda, R.D., Maheshwari, S., Milton, R.D., Minteer, S.D., Janik, M.J., Renner, J.N., and Greenlee, L.F. (2018). Catalysts for Nitrogen Reduction to Ammonia. Nat. Catal. 1, 490–500. https://doi.org/10.1038/s41929-018-0092-7.

77. Appl, M. (2012). Ammonia, 2. Production Processes. In Ullmann's Encyclopedia of Industrial Chemistry (Wiley-VCH Verlag GmbH), pp. 140–225. https://doi.org/10.1002/14356007.o02_o11.

78. Wu, L., Guo, T., and Li, T. (2020). Rational Design of Transition Metal Single-Atom Electrocatalysts: A Simulation-Based, Machine Learning-Accelerated Study. J. Mater. Chem. 8, 19290–19299. https://doi.org/10.1039/D0TA06207C.

79. Wu, L., Guo, T., and Li, T. (2021). Machine Learning-Accelerated Prediction of Overpotential of Oxygen Evolution Reaction of Single-Atom Catalysts. iScience 24, 102398. https://doi.org/10.1016/j.isci.2021.102398.

80. Wu, L., Guo, T., and Li, T. (2022). Data-Driven High-Throughput Rational Design of Double-Atom Catalysts for Oxygen Evolution and Reduction. Adv. Funct. Mater. 32, 2203439. https://doi.org/10.1002/adfm.202203439.

81. Fei, H., Dong, J., Arellano-Jiménez, M.J., Ye, G., Dong Kim, N., Samuel, E.L., Peng, Z., Zhu, Z., Qin, F., and Bao, J. (2015). Atomic Cobalt on Nitrogen-Doped Graphene for Hydrogen Generation. Nat. Commun. 6, 1–8. https://doi.org/10.1038/ncomms9668.

82. Kang, W., Lee, C.C., Jasniewski, A.J., Ribbe, M.W., and Hu, Y. (2020). Structural Evidence for a Dynamic Metallocofactor During N2 Reduction by Mo-Nitrogenase. Science 368, 1381–1385. https://doi.org/10.1126/science.aaz674.

83. Lee, C.C., Kang, W., Jasniewski, A.J., Stiebritz, M.T., Tanifuji, K., Ribbe, M.W., and Hu, Y. (2022). Evidence of Substrate Binding and Product Release Via Belt-Sulfur Mobilization of the Nitrogenase Cofactor. Nat. Catal. 5, 443–454. https://doi.org/10.1038/s41929-022-00782-7.

84. Milton, R.D., and Minteer, S.D. (2019). Nitrogenase Bioelectrochemistry for Synthesis Applications. Acc. Chem. Res. 52, 3351–3360. https://doi.org/10.1021/acs.accounts.9b00494.

85. Zheng, Y., Jiao, Y., Zhu, Y., Li, L.H., Han, Y., Chen, Y., Du, A., Jaroniec, M., and Qiao, S.Z. (2014). Hydrogen Evolution by a Metal-Free Electrocatalyst. Nat. Commun. 5, 3783–3788. https://doi.org/10.1038/ncomms4783.

86. Jiao, Y., Zheng, Y., Davey, K., and Qiao, S.Z. (2016). Activity Origin and Catalyst Design Principles for Electrocatalytic Hydrogen Evolution on Heteroatom-Doped Graphene. Nat. Energy 1, 16130–16139. https://doi.org/10.1038/nenergy.2016.130.

87. Ji, S., Wang, Z., and Zhao, J. (2019). A Boron-Interstitial Doped C2N Layer as a Metal-Free Electrocatalyst for N2 Fixation: A Computational Study. J. Mater. Chem. 7, 2392–2399. https://doi.org/10.1039/C8TA10497B.

88. Liu, X., and Dai, L. (2016). Carbon-Based Metal-Free Catalysts. Nat. Rev. Mater. 1, 16064–16112. https://doi.org/10.1038/natrevmats.2016.64.

89. Rao, C.N.R., and Chhetri, M. (2019). Borocarbonitrides as Metal-Free Catalysts for the Hydrogen Evolution Reaction. Adv. Mater. 31, 1803668. https://doi.org/10.1002/adma.201803668.

90. Navalon, S., Dhakshinamoorthy, A., Alvaro, M., Antonietti, M., and García, H. (2017). Active Sites on Graphene-Based Materials as Metal-Free Catalysts. Chem. Soc. Rev. 46, 4501–4529. https://doi.org/10.1039/C7CS00156H.

91. Légaré, M.A., Bélanger-Chabot, G., Dewhurst, R.D., Welz, E., Krummenacher, I., Engels, B., and Braunschweig, H. (2018). Nitrogen Fixation and Reduction at Boron. Science 359, 896–900. https://doi.org/10.1126/science.aaq1684.

92. Yu, X., Han, P., Wei, Z., Huang, L., Gu, Z., Peng, S., Ma, J., and Zheng, G. (2018). Boron-Doped Graphene for Electrocatalytic N2 Reduction. Joule 2, 1610–1622. https://doi.org/10.1016/j.joule.2018.06.007.

93. Shi, M.M., Bao, D., Wulan, B.R., Li, Y.H., Zhang, Y.F., Yan, J.M., and Jiang, Q. (2017). Au Sub-Nanoclusters on TiO2 toward Highly Efficient and Selective Electrocatalyst for N2 Conversion to NH3 at Ambient Conditions. Adv. Mater. 29, 1606550. https://doi.org/10.1002/adma.201606550.

94. Lv, C., Yan, C., Chen, G., Ding, Y., Sun, J., Zhou, Y., and Yu, G. (2018). An Amorphous Noble-Metal-Free Electrocatalyst That Enables Nitrogen Fixation under Ambient Conditions. Angew. Chem. Int. Ed. 130, 6181–6184. https://doi.org/10.1002/ange.201801538.

95. Chen, S., Perathoner, S., Ampelli, C., Mebrahtu, C., Su, D., and Centi, G. (2017). Electrocatalytic Synthesis of Ammonia at Room Temperature and Atmospheric Pressure from Water and Nitrogen on a Carbon-Nanotube-Based Electrocatalyst. Angew. Chem. Int. Ed. 56, 2699–2703. https://doi.org/10.1002/anie.201609533.

96. Bao, D., Zhang, Q., Meng, F.L., Zhong, H.X., Shi, M.M., Zhang, Y., Yan, J.M., Jiang, Q., and Zhang, X.B. (2017). Electrochemical Reduction of N2 under Ambient Conditions for Artificial N2 Fixation and Renewable Energy Storage Using N2/NH3 Cycle. Adv. Mater. 29, 1604799. https://doi.org/10.1002/adma.201604799.

97. Yao, Y., Zhu, S., Wang, H., Li, H., and Shao, M. (2018). A Spectroscopic Study on the Nitrogen Electrochemical Reduction Reaction on Gold and Platinum Surfaces. J. Am. Chem. Soc. 140, 1496–1501. https://doi.org/10.1021/jacs.7b12101.

98. Ling, C., Niu, X., Li, Q., Du, A., and Wang, J. (2018). Metal-Free Single Atom Catalyst for N2 Fixation Driven by Visible Light. J. Am. Chem. Soc. 140, 14161–14168. https://doi.org/10.1021/jacs.8b07472.

99. Liu, J., Liu, Y., Liu, N., Han, Y., Zhang, X., Huang, H., Lifshitz, Y., Lee, S.T., Zhong, J., and Kang, Z. (2015). Metal-Free Efficient Photocatalyst for Stable Visible Water Splitting Via a Two-Electron Pathway. Science 347, 970–974. https://doi.org/10.1126/science.aaa3145.

100. Wang, X., Maeda, K., Thomas, A., Takanabe, K., Xin, G., Carlsson, J.M., Domen, K., and Antonietti, M. (2009). A Metal-Free Polymeric Photocatalyst for Hydrogen Production from Water under Visible Light. Nat. Mater. 8, 76–80. https://doi.org/10.1038/nmat2317.

101. Zhu, J., Wei, Y., Chen, W., Zhao, Z., and Thomas, A. (2010). Graphitic Carbon Nitride as a Metal-Free Catalyst for No Decomposition. Chem. Commun. 46, 6965–6967. https://doi.org/10.1039/C0CC01432J.

102. Lv, X., Wei, W., Li, F., Huang, B., and Dai, Y. (2019). Metal-Free B@g-CN: Visible/Infrared Light-Driven Single Atom Photocatalyst Enables Spontaneous Dinitrogen Reduction to Ammonia. Nano Lett. 19, 6391–6399. https://doi.org/10.1021/acs.nanolett.9b02572.

103. Liu, C., Li, Q., Wu, C., Zhang, J., Jin, Y., MacFarlane, D.R., and Sun, C. (2019). Single-Boron Catalysts for Nitrogen Reduction Reaction. J. Am. Chem. Soc. 141, 2884–2888. https://doi.org/10.1021/jacs.8b13165.

104. Wang, M., Liu, S., Qian, T., Liu, J., Zhou, J., Ji, H., Xiong, J., Zhong, J., and Yan, C. (2019). Over 56.55% Faradaic Efficiency of Ambient Ammonia Synthesis Enabled by Positively Shifting the Reaction Potential. Nat. Commun. 10, 341. https://doi.org/10.1038/s41467-018-08120-x.

105. Zang, W., Yang, T., Zou, H., Xi, S., Zhang, H., Liu, X., Kou, Z., Du, Y., Feng, Y.P., Shen, L., et al. (2019). Copper Single Atoms Anchored in Porous Nitrogen-Doped Carbon as Efficient Ph-Universal Catalysts for the Nitrogen Reduction Reaction. ACS Catal. 9, 10166–10173. https://doi.org/10.1021/acscatal.9b02944.

106. Zhao, W., Zhang, L., Luo, Q., Hu, Z., Zhang, W., Smith, S., and Yang, J. (2019). Single Mo1(Cr1) Atom on Nitrogen-Doped Graphene Enables Highly Selective Electroreduction of Nitrogen into Ammonia. ACS Catal. 9, 3419–3425. https://doi.org/10.1021/acscatal.8b05061.

107. Liu, J.H., Yang, L.M., and Ganz, E. (2019). Electrocatalytic Reduction of CO2 by Two-Dimensional Transition Metal Porphyrin Sheets. J. Mater. Chem. 7, 11944–11952. https://doi.org/10.1039/C9TA01188A.

108. Wang, H.Y., Weng, C.C., and Yuan, Z.Y. (2021). Insights into Efficient Transition Metal-Nitrogen/Carbon Oxygen Reduction Electrocatalysts. J. Energy Chem. 56, 470–485. https://doi.org/10.1016/j.jechem.2020.08.030.

109. Tylus, U., Jia, Q., Strickland, K., Ramaswamy, N., Serov, A., Atanassov, P., and Mukerjee, S. (2014). Elucidating Oxygen Reduction Active Sites in Pyrolyzed Metal–Nitrogen Coordinated Non-Precious-Metal Electrocatalyst Systems. J. Phys. Chem. C 118, 8999–9008. https://doi.org/10.1021/jp500781v.

110. Varela, A.S., Ju, W., Bagger, A., Franco, P., Rossmeisl, J., and Strasser, P. (2019). Electrochemical Reduction of CO2 on Metal-Nitrogen-Doped Carbon Catalysts. ACS Catal. 9, 7270–7284. https://doi.org/10.1021/acscatal.9b01405.

111. Zagal, J.H., Specchia, S., and Atanassov, P. (2021). Mapping Transition Metal-Mn4 Macrocyclic Complex Catalysts Performance for the Critical Reactivity Descriptors. Curr. Opin. Electrochem. 27, 100683. https://doi.org/10.1016/j.coelec.2020.100683.

112. He, T., Chen, S., Ni, B., Gong, Y., Wu, Z., Song, L., Gu, L., Hu, W., and Wang, X. (2018). Zirconium–Porphyrin-Based Metal–Organic Framework Hollow Nanotubes for Immobilization of Noble-Metal Single Atoms. Angew. Chem. Int. Ed. 130, 3551–3556. https://doi.org/10.1002/ange.201800817.

113. Wang, X., Chen, W., Zhang, L., Yao, T., Liu, W., Lin, Y., Ju, H., Dong, J., Zheng, L., Yan, W., et al. (2017). Uncoordinated Amine Groups of Metal–Organic Frameworks to Anchor Single Ru Sites as Chemoselective Catalysts toward the Hydrogenation of Quinoline. J. Am. Chem. Soc. 139, 9419–9422. https://doi.org/10.1021/jacs.7b01686.

114. He, X., He, Q., Deng, Y., Peng, M., Chen, H., Zhang, Y., Yao, S., Zhang, M., Xiao, D., Ma, D., et al. (2019). A Versatile Route to Fabricate Single Atom Catalysts with High Chemoselectivity and Regioselectivity in Hydrogenation. Nat. Commun. 10, 3663. https://doi.org/10.1038/s41467-019-11619-6.

115. Nakamura, Y., Aratani, N., Shinokubo, H., Takagi, A., Kawai, T., Matsumoto, T., Yoon, Z.S., Kim, D.Y., Ahn, T.K., Kim, D., et al. (2006). A Directly Fused Tetrameric Porphyrin Sheet and Its Anomalous Electronic Properties That Arise from the Planar Cyclooctatetraene Core. J. Am. Chem. Soc. 128, 4119–4127. https://doi.org/10.1021/ja057812l.

116. Tanaka, T., and Osuka, A. (2015). Conjugated Porphyrin Arrays: Synthesis, Properties and Applications for Functional Materials. Chem. Soc. Rev. 44, 943–969. https://doi.org/10.1039/C3CS60443H.

117. Yao, X., Chen, Z.W., Wang, Y.R., Lang, X.Y., Zhu, Y.F., Gao, W., and Jiang, Q. (2020). High-Loading Intrinsic Active Sites for Ammonia Synthesis Using Efficient Single-Atom Catalyst: 2D Tungsten-Porphyrin Sheet. Appl. Surf. Sci. 529, 147183. https://doi.org/10.1016/j.apsusc.2020.147183.

118. Luo, G., Wang, Y., and Li, Y. (2017). Two-Dimensional Iron-Porphyrin Sheet as a Promising Catalyst for Oxygen Reduction Reaction: A Computational Study. Sci. Bull. 62, 1337–1343. https://doi.org/10.1016/j.scib.2017.08.015.

119. Liu, S., Dhar, P., Wu, J.D., Tan, Y., Cheng, Z., Shen, Z., and Fan, M. (2019). Two-Dimensional Transition Metal Porphyrin Sheets as a Promising Single-Atom-Catalyst for Dinitrogen Electrochemical Reduction to Ammonia: A Theoretical Study. J. Clin. Med. 8, 1492–1499. https://doi.org/10.1021/acs.jpcc.9b10294.

120. Impeng, S., Roongcharoen, T., Maitarad, P., Wu, H., Chitpakdee, C., Promarak, V., Shi, L., and Namuangruk, S. (2020). High Selective Catalyst for Ethylene Epoxidation to Ethylene Oxide: A DFT Investigation. Appl. Surf. Sci. 513, 145799. https://doi.org/10.1016/j.apsusc.2020.145799.

121. Klet, R.C., Wang, T.C., Fernandez, L.E., Truhlar, D.G., Hupp, J.T., and Farha, O.K. (2016). Synthetic Access to Atomically Dispersed Metals in Metal–Organic Frameworks Via a Combined Atomic-Layer-Deposition-in-Mof and Metal-Exchange Approach. Chem. Mater. 28, 1213–1219. https://doi.org/10.1021/acs.chemmater.5b04887.

122. Zhang, H., Hwang, S., Wang, M., Feng, Z., Karakalos, S., Luo, L., Qiao, Z., Xie, X., Wang, C., Su, D., et al. (2017). Single Atomic Iron Catalysts for Oxygen Reduction in Acidic Media: Particle Size Control and Thermal Activation. J. Am. Chem. Soc. 139, 14143–14149. https://doi.org/10.1021/jacs.7b06514.

123. Manzeli, S., Ovchinnikov, D., Pasquier, D., Yazyev, O.V., and Kis, A. (2017). 2D Transition Metal Dichalcogenides. Nat. Rev. Mater. 2, 17033–17115. https://doi.org/10.1038/natrevmats.2017.33.

124. Wang, Q.H., Kalantar-Zadeh, K., Kis, A., Coleman, J.N., and Strano, M.S. (2012). Electronics and Optoelectronics of Two-Dimensional Transition Metal Dichalcogenides. Nat. Nanotechnol. 7, 699–712. https://doi.org/10.1038/nnano.2012.193.

125. Fu, Q., Han, J., Wang, X., Xu, P., Yao, T., Zhong, J., Zhong, W., Liu, S., Gao, T., Zhang, Z., et al. (2021). 2D Transition Metal Dichalcogenides: Design, Modulation, and Challenges in Electrocatalysis. Adv. Mater. 33, 1907818. https://doi.org/10.1002/adma.201907818.

126. Yao, X., Wang, Z., Zhang, H., Zhu, Y., and Jiang, Q. (2019). Thickness-Dependent Bandgap of Transition Metal Dichalcogenides Dominated by Interlayer Van Der Waals Interaction. Physica E 113, 11–19. https://doi.org/10.1016/j.physe.2018.12.037.

127. Choi, W., Choudhary, N., Han, G.H., Park, J., Akinwande, D., and Lee, Y.H. (2017). Recent Development of Two-Dimensional Transition Metal Dichalcogenides and Their Applications. Mater. Today 20, 116–130. https://doi.org/10.1016/j.mattod.2016.10.002.

128. Mak, K.F., and Shan, J. (2016). Photonics and Optoelectronics of 2D Semiconductor Transition Metal Dichalcogenides. Nat. Photonics 10, 216–226. https://doi.org/10.1038/nphoton.2015.282.

129. Yao, X., Wang, Y.R., Lang, X.Y., Zhu, Y.F., and Jiang, Q. (2020). Composition-and Layer-Dependent Bandgap of Two-Dimensional Transition Metal Dichalcogenides Alloys. Physica E 124, 114243. https://doi.org/10.1016/j.physe.2020.114243.

130. Yu, Z., Pan, Y., Shen, Y., Wang, Z., Ong, Z.Y., Xu, T., Xin, R., Pan, L., Wang, B., Sun, L., et al. (2014). Towards Intrinsic Charge Transport in Monolayer Molybdenum Disulfide by Defect and Interface Engineering. Nat. Commun. 5, 5290. https://doi.org/10.1038/ncomms6290.

131. Radisavljevic, B., Radenovic, A., Brivio, J., Giacometti, V., and Kis, A. (2011). Single-Layer MoS2 Transistors. Nat. Nanotechnol. 6, 147–150. https://doi.org/10.1038/nnano.2010.279.

132. Hong, J., Hu, Z., Probert, M., Li, K., Lv, D., Yang, X., Gu, L., Mao, N., Feng, Q., Xie, L., et al. (2015). Exploring Atomic Defects in Molybdenum Disulphide Monolayers. Nat. Commun. 6, 6293. https://doi.org/10.1038/ncomms7293.

133. Yao, X., Chen, Z., Wang, Y., Lang, X., Gao, W., Zhu, Y., and Jiang, Q. (2019). Activated Basal Planes of WS2 by Intrinsic Defects as Catalysts for the Electrocatalytic Nitrogen Reduction Reaction. J. Mater. Chem. 7, 25961–25968. https://doi.org/10.1039/C9TA10050D.

134. Li, L., Li, B., Guo, Q., and Li, B. (2019). Theoretical Screening of Single-Atom-Embedded Mosse Nanosheets for Electrocatalytic N2 Fixation. J. Phys. Chem. C 123, 14501–14507. https://doi.org/10.1021/acs.jpcc.9b02657.

135. Ma, X., Zhang, H.M., Liu, Y.Q., Li, D., Lv, H., He, H., and Huang, C. (2019). N2 Reduction Using Single Transition-Metal Atom Supported on Defective WS2 Monolayer as Promising Catalysts: A DFT Study. Appl. Surf. Sci. 41, 684–685. https://doi.org/10.1016/j.apsusc.2019.05.022.

136. Xu, J., Shao, G., Tang, X., Lv, F., Xiang, H., Jing, C., Liu, S., Dai, S., Li, Y., Luo, J., and Zhou, Z. (2022). Frenkel-Defected Monolayer MoS2 Catalysts for Efficient Hydrogen Evolution. Nat. Commun. 13, 2193. https://doi.org/10.1038/s41467-022-29929-7.

137. Lahiri, N., Lotfizadeh, N., Tsuchikawa, R., Deshpande, V.V., and Louie, J. (2017). Hexaaminobenzene as a Building Block for a Family of 2D Coordination Polymers. J. Am. Chem. Soc. 139, 19–22. https://doi.org/10.1021/jacs.6b09889.